AD_______________

Award Number: W81XWH-10-1-0041

TITLE: Understanding the Etiology of Tuberous Sclerosis Complex

PRINCIPAL INVESTIGATOR: Angélique Bordey, Ph.D.

CONTRACTING ORGANIZATION: Yale University
New Haven, CT 0652

REPORT DATE: July 2012

TYPE OF REPORT: Annual

PREPARED FOR: U.S. Army Medical Research and Materiel Command
Fort Detrick, Maryland 21702-5012

DISTRIBUTION STATEMENT: Approved for Public Release;
Distribution Unlimited

REPORT DOCUMENTATION PAGE

Form Approved
OMB No. 0704-0188

1. REPORT DATE July 2012	**2. REPORT TYPE** Annual	**3. DATES COVERED** 1 July 2011 – 30 June 2012

4. TITLE AND SUBTITLE

Understanding the Etiology of Tuberous Sclerosis Complex

5a. CONTRACT NUMBER

5b. GRANT NUMBER
W81XWH-10-1-0041

5c. PROGRAM ELEMENT NUMBER

6. AUTHOR(S)

Angélique Bordey, Ph.D.

E-Mail: angelique.bordey@yale.edu

5d. PROJECT NUMBER

5e. TASK NUMBER

5f. WORK UNIT NUMBER

7. PERFORMING ORGANIZATION NAME(S) AND ADDRESS(ES)

Yale University
New Haven, CT 0652

8. PERFORMING ORGANIZATION REPORT NUMBER

9. SPONSORING / MONITORING AGENCY NAME(S) AND ADDRESS(ES)
U.S. Army Medical Research and Materiel Command
Fort Detrick, Maryland 21702-5012

10. SPONSOR/MONITOR'S ACRONYM(S)

11. SPONSOR/MONITOR'S REPORT NUMBER(S)

12. DISTRIBUTION / AVAILABILITY STATEMENT
Approved for Public Release; Distribution Unlimited

13. SUPPLEMENTARY NOTES

14. ABSTRACT

Tuberous Sclerosis Complex (TSC) is a genetic multisystem disorder characterized by severe neurological symptoms (e.g. seizures), which are the most significant causes of disability and morbidity. Presently, there are no known cures for TSC and the etiology of the disease is not well understood, perhaps due to the lack of model system to study this disorder. In TSC patients, mutations in Tsc1 or Tsc2, result in the formation of lesions. The mechanisms leading to TSC lesions and associated seizure generation during perinatal life remain unclear in the absence of an animal model of TSC lesions. The goal of our recent ongoing funding cycle based on our Statement of Work was to generate TSC lesions using a new approach in transgenic Tsc1 mice (Task 1) and to assess at which developmental stages some of the defects start to occur following Tsc1 inactivation (Task 2). These two Tasks have been achieved in due time as proposed in our Timeline. Using a novel technical approach (i.e. in vivo electroporation in mice with conditional and mutant alleles) we generated the first TSC animal model that replicates the discrete cortical lesions seen in humans. We have gathered information on the mechanisms of lesion formation and cortical hyperexcitability. This latter work is undergoing. We have published our findings in a research article and have also published a News and Views regarding this article. We have presented our data at several meetings.

15. SUBJECT TERMS
Tuberous Sclerosis, cortical tubers

16. SECURITY CLASSIFICATION OF:			**17. LIMITATION OF ABSTRACT**	**18. NUMBER OF PAGES**	**19a. NAME OF RESPONSIBLE PERSON** USAMRMC
a. REPORT U	**b. ABSTRACT** U	**c. THIS PAGE** U	UU	56	**19b. TELEPHONE NUMBER** *(include area code)*

Table of Contents

Page

Introduction

Tuberous Sclerosis Complex (TSC) is a genetic multisystem disorder characterized by severe neurological symptoms (e.g. seizures), which are the most significant causes of disability and morbidity. Presently, there are no known cures for TSC and the etiology of the disease is not well understood, perhaps due to the lack of model system to study this disorder. In TSC patients, mutations in one of two tumor suppressor genes, *Tsc1* or *Tsc2,* result in the formation of lesions. The mechanisms leading to TSC lesions and associated seizure generation during perinatal life remain unclear. We proposed to test the hypothesis that deletion of Tsc genes in perinatal neural progenitor cells contributes to the generation of TSC lesions, and we propose to identify the mechanisms underlying that process.

To test our hypothesis, we have used a double hit model in transgenic mice carrying conditional (fl) and mutant (mut, non-functional) *Tsc1* alleles ($Tsc1^{fl/mut}$ mice) by deleting the conditional *Tsc1* allele in embryonic and neonatal progenitor cells using *in vivo* electroporation of Cre recombinase-containing plasmids. We had proposed the following two aims.

First, we proposed to test whether deletion of *Tsc1* in perinatal progenitor cells generates TSC lesions (i.e. cortical tubers with giant cells and subependymal nodules, olfactory heterotopia) to get insights into the mechanisms of lesion formation. The second aim was to study the mechanism of cortical hyperexcitability and identify some of the mechanisms leading to lesion formation. We would then test the effects of inhibiting and knocking down selective molecules on lesion formation and cortical excitability.

We have entirely completed aim 1 as originally proposed in our Statement of Work. Using a novel technical approach (i.e. *in vivo* electroporation in mice with conditional and mutant alleles), we described first TSC animal model that replicates the discrete cortical and olfactory lesions and subependymal nodules as seen in humans. We have gathered information on the mechanisms of lesion formation (e.g. hypoxia induced factor 1, Hif1) and cortical hyperexcitability. We are finishing this latter work. We have published our findings in research articles and have presented our data at several meetings.

Body

Background

Epilepsy and cortical lesions

Epilepsy is observed in 75% of affected TSC individuals. Seizures often begin during the first year of life as infantile spasms that are unresponsive to conventional anti-epileptic drug therapies (Curatolo et al., 2001; Holmes and Stafstrom, 2007).

Seizures in TSC individuals are associated with cortical lesions or malformations called tubers (Thiele, 2004) (**Figure 1**). Indeed, seizures have a focal or multifocal origin with a topographic correspondence between EEG foci and MRI high signal lesions, demonstrating the preponderant role of cortical tubers as epileptogenic foci (Jansen et al., 2007; Jansen et al., 2008). Resecting tubers in pharmacologically intractable epileptic patients with TSC reduces or eliminates seizure activity in a subpopulation of these patients (Jansen et al., 2007; Jensen, 2009). However, how a tuber forms and contributes to cortical hyperexcitability remains unclear in the absence of a reliable animal model of cortical tubers. One of our major objectives was thus to generate cortical tubers which we have successfully accomplished last year. The work was already reviewed and published.

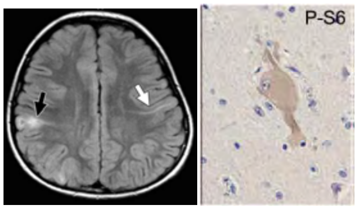

Figure 1: Cortical tubers (Left panel, black arrow) are discrete focal lesions, which can be detected by MRI.
Right panel: elevated S6 phosphorylation (pS6, brown) is a hallmark of cytomegalic neurons present in tubers.

We are in the process of analyzing our data regarding cortical excitability in and around a tuber. These data are not presented and were the subject of a oral presentation by my postdoctoral fellow, Dr. Feliciano, at the Young Investigator workshop of the American Epilepsy meeting (Baltimore, 2012).

Subependymal nodules and heterotopia in olfactory structures

Other brain lesions observed in TSC patients are subependymal (SE) nodules along the lateral ventricle and heterotopia in olfactory structures. The function of these nodules remains unclear in terms of their contribution to network excitability (DiMario, Jr., 2004; Mizuguchi and Takashima, 2001). Nevertheless, the nodules transform into subependymal giant cell astrocytoma (SEGA) in 5-15% of the patients and need to be resected when they lead to hydrocephalus by preventing fluid circulation in the ventricle.

Considering that gliogenesis and neurogenesis persist beyond birth in the subependymal zone (SEZ) (Pathania et al., 2010), we hypothesized that SE nodules and olfactory heterotopia arise from neonatal SEZ progenitor cells expressing mutations in *Ts1* or *Tsc2*. During the first two weeks after birth in mice (~8-12 months in humans), SEZ neural progenitor cells contribute to extensive gliogenesis (Levison and Goldman, 1993) as well as olfactory bulb. ***Generating SEZ nodules and heterotopia was a part of aim 1. This work has been accomplished and is described below in our research accomplishments.***

In addition, we used this newly developed model system of heterotopia toidentify downstream molecules responsible for abnormal cell development. Below we will present data on Hif1.

Our research accomplishments

The goal of our recent ongoing funding cycle based on our Statement of Work was to finish ongoing work regarding the generation of TSC lesions from neonatal neural progenitor cells (NPCs) in the SVZ (part of Task 1), to assess cortical excitability in the presence of tubers (Task 3, not presented here because under analysis) and to start identifying molecules responsible for TSC lesions (Task 4). These Tasks have been achieved in due time as proposed in our Timeline. Data obtained are detailed below.

Generation of TSC lesions from NPCs in the SVZ

To examine whether postnatal neurogenesis contributes to SE nodules and SEGA, we used conditional transgenic mice as recently reported to induce SVZ nodules and SEGA (Zhou et al., 2011). Loss of heterozygosity in SVZ cells was achieved using mice expressing *Tsc1* alleles flanked by LoxP sites (floxed, fl) crossed with nestin-CreER^{T2}/R26R-YFP mice to generate *Tsc1*$^{fl/fl}$/nestin^{CreERT2} mice (**Fig. 1A**) (Meikle et al., 2007; Lagace et al., 2007). These nestin-CreER^{T2} mice have been used to induce selective recombination in cells of the neurogenic zones in adults (Shuang et al., 2004). In neonates, nestin is also expressed in astrocytes and progressively disappears as they mature and acquire glial fibrillary acidic protein GFAP in rodents. Upon tamoxifen injection in *Tsc1*$^{fl/fl}$/nestin^{CreERT2}, nestin-expressing cells, including SVZ cells and astrocytes, are expected to lose *Tsc1* and express YFP. Control mice were *Tsc1*$^{fl/wt}$/nestin^{CreERT2} (wildtype, wt).

Tamoxifen was injected at P7 (2 injections) and brains were collected at postnatal day (P) 28. *Tsc1*$^{fl/fl}$/nestin^{CreERT2} mice displayed GFAP- and RC2-rich SEGA-like lesions in the ventral SVZ (**Fig. 1C**, GFAP not shown, location shown on the diagram in **Fig. 1B** at the base of the ventricle) (Zhou et al., 2011). RC2 is a radial glial cell marker (Misson et al., 1988). These data suggest that SEGA can form during the neonatal period from SVZ NPCs.

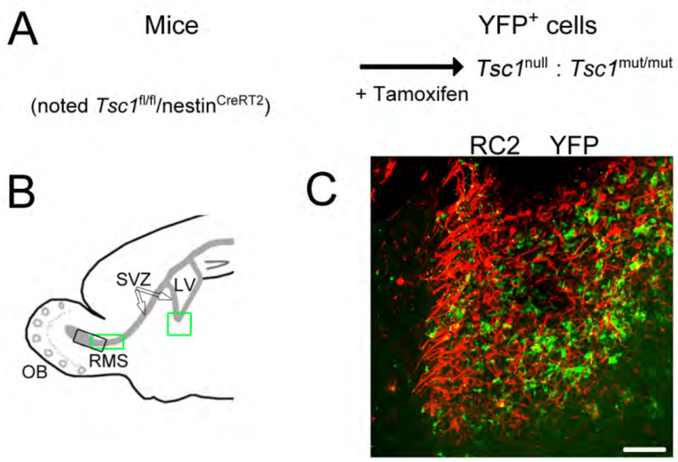

Figure 2. Postnatal deletion of *Tsc1* using inducible transgenic mice. (A) Diagram illustrating the inducible transgenic mouse line used to delete *Tsc1* (*i.e.* null) and express YFP in nestin-expressing cells and their progeny following tamoxifen injection at postnatal day (P) 7. **(B)** Diagram illustrating the locations of the images shown in C on a sagittal section. LV: lateral ventricle; SVZ: subventricular zone. OB: olfactory bulb; RMS: rostral migratory stream. **(C)** P28 image of RC2 (red)-rich SVZ nodule containing YFP$^+$ *Tsc1*^{null} cells following tamoxifen-induced recombination at P7. Scale bar: 70 µm.

To examine whether the neonatal NPCs could also generate focal olfactory lesions, we used neonatal electroporation. This approach allows precise targeting of plasmids into NPCs lining the lateral ventricle (Lacar et al., 2010). These NPCs generate neurons that migrate to the olfactory bulb via the RMS and are synaptically mature by 3-4 weeks after birth (Petreanu and Alvarez-Buylla, 2002). We used *Tsc1* mice crossed with R26R-Stop-RFP mice (RFP, red fluorescent protein for tdTomato). In *Tsc1*$^{\mathrm{fl/mut}}$/RFP mice, Cre recombinase (Cre) expression is expected to lead to TSC1 loss and RFP expression (**Fig. 3A**). RFP^{+} neurons are thus expected to be *Tsc1*$^{\mathrm{null}}$ while surrounding RFP^{-} neurons are *Tsc1*$^{\mathrm{haplo}}$ (haplo for haploinsufficient).

A Cre- and GFP-encoding plasmid were electroporated into SVZ progenitor cells at P0-1 resulting in visible GFP fluorescence 1-day post-electroporation (**Fig. 3B and C**) (Lacar et al., 2010; Platel et al., 2010). GFP allows to birth-mark neurons born during the first 7-10 days post-electroporation because GFP is diluted as cells divide while RFP is permanently expressed (Lacar et al., 2010)(**Fig. 3D**). As a result, RFP^{+} but not GFP^{+} newborn neurons continuously accumulate in the circuit (**Fig. 3E**). We reported that *Tsc1* was deleted from newborn neurons leading to mTOR pathway activation and cytomegally (please see Appendix for manuscript).

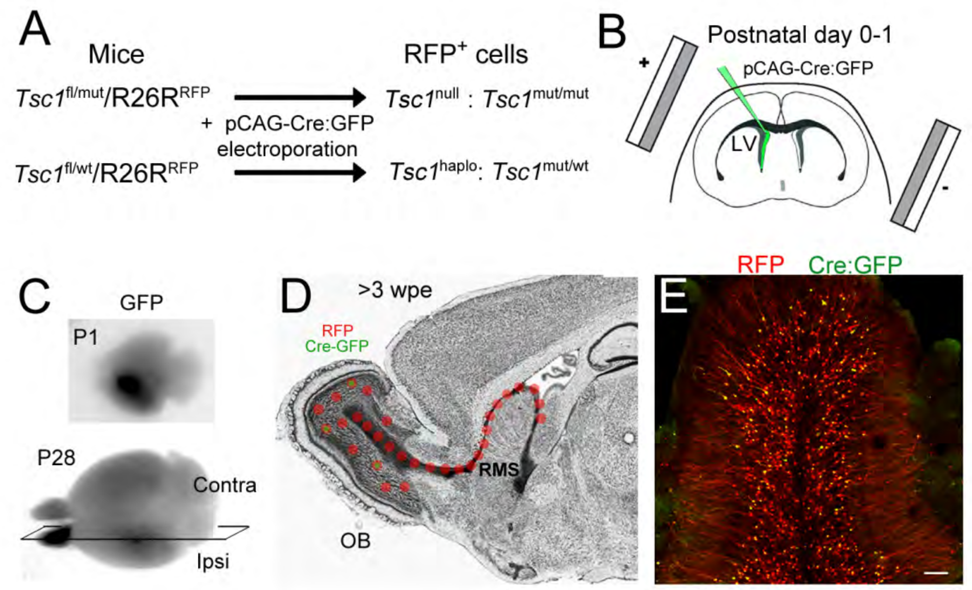

Figure 3. Postnatal deletion of *Tsc1* using neonatal electroporation and the Cre-Lox system. (A) Schematic describing the loss of one or two *Tsc1* alleles in cells containing a plasmid encoding Cre:GFP under the CAG promoter that is expressed through neonatal electroporation in *Tsc1*$^{\mathrm{fl/wt}}$/R26R and *Tsc1*$^{\mathrm{fl/mut}}$/R26R, respectively. Cells containing the pCAG-Cre:GFP also express RFP. **(B)** Diagram illustrating the principle of neonatal electroporation of a plasmid into neural progenitor cells lining the lateral ventricle. **(C)** Images of P1 and P28 fixed brains containing RFP^{+} cells in the ipsilateral olfactory bulb. **(D)** Diagram illustrating the migratory path and final location of newly born cells 3 weeks post-electroporation (wpe). RFP expression persists permanently due to its genomic integration (R26R mice) while GFP expression from either a pCAG-GFP or pCAG-Cre:GFP is diluted in newly born cells due to successive cell division. As a result, only cells born during the first 7-10 days express GFP. **(E)** Confocal image of RFP^{+} and GFP^{+} newly born cells in a coronal olfactory bulb section. RFP^{+}/GFP^{+} cells outnumber RFP^{+}/GFP^{-} cells. Scale bar: 70 µm.

Next we examined sections from electroporated mice at P0.

We first examined on the migratory pathway to the olfactory bulb. Gross examination of sagittal sections from P28 *Tsc1*$^{fl/mut}$ mice revealed the presence of migratory heterotopia, defined by the ectopic location or misplacement of groups of *Tsc1*^{null} cells. Examination of sagittal sections at low magnification led us identify heterotopia in all animals examined (n=13) that were found at three major locations: in the RMS both at its entry point caudally and at the interface RMS and RMS-OB, in the RMS-OB and adjacent to the RMS in the AON as well as near the anterior commissure olfactory limb (**Fig. 4A and B**, green rectangles indicate the location of heterotopia). No migratory heterotopias were visible in electroporated *Tsc1*$^{fl/wt}$/R26R mice (data not shown).

Closer examination of the heterotopia revealed two categories, some with an apparent mixed neuroglial phenotype (**Fig. 4C-G**) and some with a neuronal phenotype (**Fig. 4H and I**). The mixed neuroglial phenotype was visible due to the presence of a meshwork of lamelipodia-like processes giving a nodular appearance or the presence of cells with neuronal or glial morphology (**Fig. 4C**). Heterotopia with a lamelipodia-like structure were preferentially found in the AON as shown in Figure 4B and 4C. Heterotopia in the RMS and RMS-OB displayed cells with an astrocytic (bushy), a neuronal morphology or an undifferentiated morphology (**Fig. 4D-G**). Cells with a neuronal morphology displayed extensive dendrites with spines and a thin process identified as an axon by the presence of varicosities (white arrows, **Fig. 4E-G**). Cells forming the heterotopia displayed enlarged cells body compared to surrounding cells, in particular doublecortin (DCX)-immunopositive neuroblasts in the RMS (**Fig. 4F and G**, DCX staining not shown).

Mixed phenotype-heterotopia comprised GFP$^+$ and GFP$^-$/RFP$^+$ cells. In wild-type mice, GFP$^+$ cells, which are born between P0 and P10, should have reached the olfactory bulb by P28 (see (Lacar et al., 2010) for more details). Indeed in *Tsc1*$^{fl/wt}$/R26R mice, only 8% of the RFP$^+$ cells were GFP$^+$ in the RMS (23/250 cells, n=3 mice). By contrast, we found that 22% of *Tsc1*^{null} RFP$^+$ cells were GFP$^+$ cells in the RMS (280/1092 cells, n=3, p<0.0001, Fisher's Exact test). Thus, heterotopia contained early born GFP$^+$ cells that are stalled in the RMS and may thus trap late born cells as well as disrupt their migratory path.

Heterotopia comprised of 3-15 cytomegalic neurons were also visible along the RMS-OB and more specifically, in the anterior commissure olfactory limb (**Fig. 4H and I**). These cells displayed a neuronal morphology, and were NeuN- and pS6-immunopositive (data not shown). The majority of these ectopic neurons were GFP$^+$ and thus early born (**Fig. 4H**).

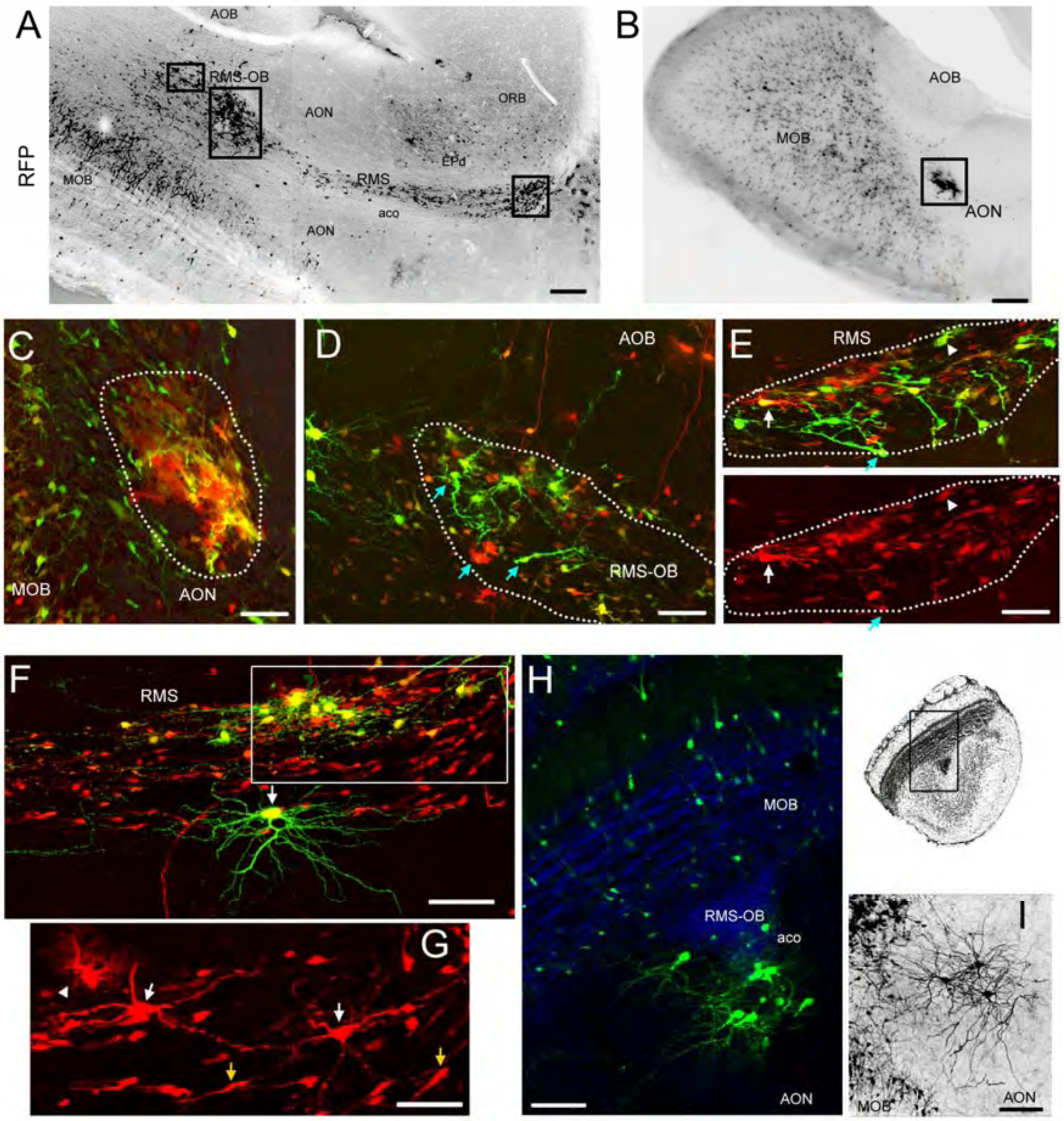

Figure 4. *Tsc1*$^{\mathrm{null}}$ cells form migratory heterotopia in and out of the RMS. (A and B) low magnification photographs of RMS/RMS-OB (A) and AON (B) lesions containing RFP$^+$ cells in sagittal sections of *Tsc1*$^{\mathrm{fl/mut}}$/R26R mice electroporated at P1 with pCAG-Cre:GFP and pCAG-GFP. The green rectangles illustrate the approximate locations of images shown in C-E. **(C)** Confocal image of a lesion in the AON, the location of which is shown in B. The lesion contains RFP$^+$/GFP$^+$ and RFP$^+$/GFP$^-$ cells. **(D-G)** Confocal Z-stack images of lesions in the RMS-OB (D) and RMS (E and F), the locations of which are shown in A. G is a zoom and smaller Z-stack of the region in the white rectangle in F. Blue arrows (D and E) point to cells with an immature morphology. White arrows (E, F, and G) point to some neurons. Arrowhead (E and G) points to examples of cells resembling astrocytes. Yellow arrows (in G) point to neuroblasts. **(H and I)** Confocal Z-stack images of neuronal heterotopias in the aco of the olfactory bulb in a coronal section (GFP$^+$ neurons in green, DAPI in blue, H) and neuronal heterotopia in the AON (black, I). Scale bars: 700 µm (A and B), 40 µm (C), 35 µm (D), 50 µm (E and G), 70 µm (F, H, and I). aco: anterior commissure, olfactory limb; AOB: accessory olfactory bulb; AON: accessory olfactory nucleus; aco: EP: doral endopiriform cortex; ORB: orbital cortex.

Upon entering the olfactory bulb, the majority of newborn neurons integrate in the granule cell layer. Next, we examined the overall organization of granule cells and their dendritic arbor. In sagittal sections there was a apparent clumping of cytomegalic *Tsc1*$^{\text{null}}$ cells (**Fig. 5B**), while *Tsc1*$^{\text{haplo}}$ cells were equally distributed (**Fig. 5A**). To quantify the disorganization of granule cells, we performed nearest neighbor calculations in which the density of cells and the distance between each were measured (**Fig. 5C**). These measurements were compared to a theoretical Poisson distribution. The difference between the theoretical and experimental values in *Tsc1*$^{\text{fl/mut}}$/R26R mice was significantly lower than that in *Tsc1*$^{\text{fl/wt}}$/R26R mice (R=4.2 ± 1.2, n=10 versus R = 9.0 ± 1.5, n=12 sections, **Fig. 5D**) suggesting a decreased organization in the *Tsc1*$^{\text{fl/mut}}$ olfactory bulb ($p<0.05$).

Another observation in coronal sections was the hypertrophic dendritic tree of *Tsc1*$^{\text{null}}$ granule neurons (**Fig. 5E**). Using Scholl analysis of the proximal dendrites, we found that the number of dendritic crossings was increased in *Tsc1*$^{\text{null}}$ compared to *Tsc1*$^{\text{haplo}}$ neurons (**Fig. 5F**). Since ultimate circuit formation and function depend on proper cell placement and morphogenesis, we expect abnormal circuit activity.

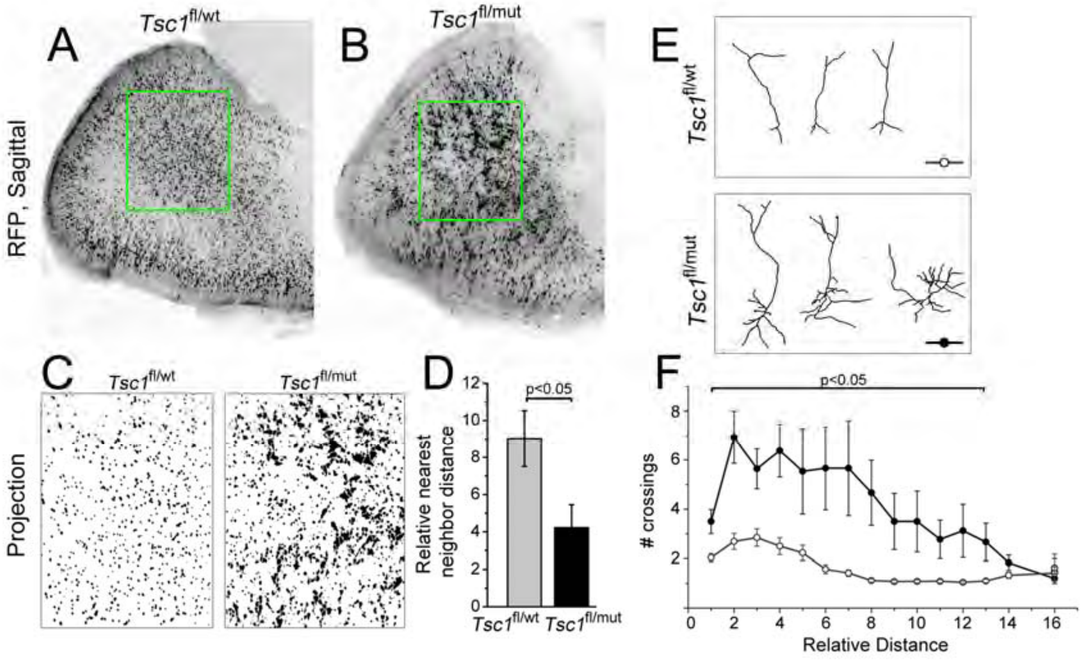

Figure 5. *Tsc1*$^{\text{null}}$ neurons form micronodules throughout the olfactory bulb and hypertrophic dendrites. (A and B) Confocal images of RFP^{+} cells in olfactory bulb sagittal sections from *Tsc1*$^{\text{fl/wt}}$/R26R (A) and *Tsc1*$^{\text{fl/mut}}$/R26R mice (B). **(C)** Projections of the RFP signals in the green square in A and B. **(D)** Bar graph of the relative nearest neighbor distance for RFP^{+} cells in the olfactory bulb of *Tsc1*$^{\text{fl/wt}}$/R26R (grey) and *Tsc1*$^{\text{fl/mut}}$/R26R (black) mouse. **(E)** Representative reconstructions of RFP^{+} olfactory neurons in sections from *Tsc1*$^{\text{fl/wt}}$/R26R and *Tsc1*$^{\text{fl/mut}}$/R26R mice. **(F)** Corresponding plots of the number of crossing as a function of the distance from the soma (n=14 cells for each plot). Filled circles: *Tsc1*$^{\text{fl/mut}}$/R26R mice.

While examining sections of *Tsc1*$^{fl/mut}$ brains, we found GFP^{+} neurons in the nucleus accumbens and in the cortex (**Fig. 6**). The majority of neurons were GFP^{+} suggesting that they were born during the neonatal period. Such neurons were absent in *Tsc1*$^{fl/wt}$ brain or very rare (1 per section occasionally). In the nucleus accumbens, neurons were located at the base of the lateral ventricle and around the anterior commissure (**Fig. 6B and C**). GFP^{+} cells were identified as neurons based on NeuN immunostaining. In the cortex, 10-15 neurons were found per sections. Neurons occurred in clusters of 2-6, and were located in the deep cortical layers and in layer II **(Fig. 6D-I)**. Cortical neurons display an extensive dendritic tree with spines as well as a thin process with varicosities resembling an axon.

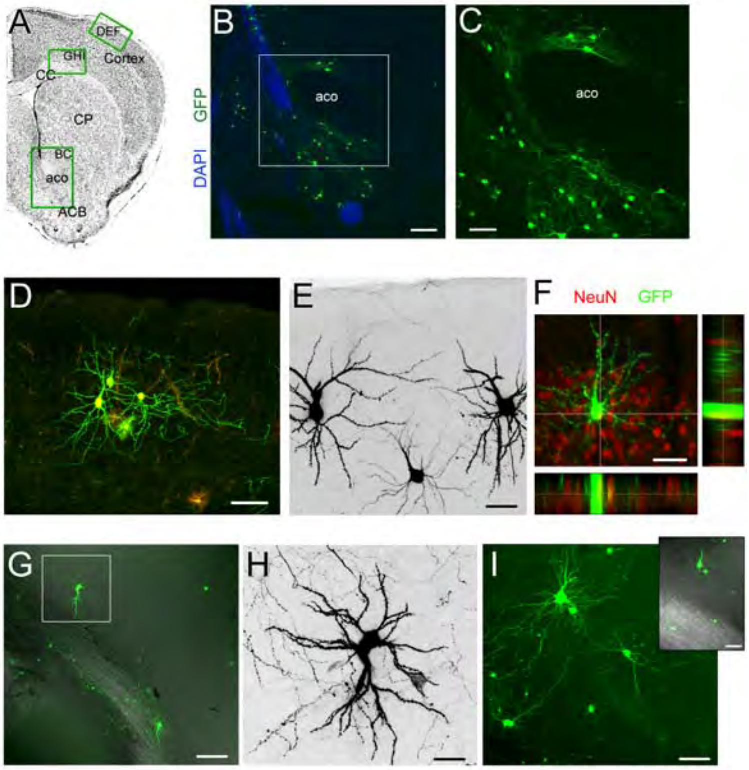

Figure 6. Newborn *Tsc1*^{null} neurons are rerouted to cortical and subcortical areas. (A) Coronal sections with green rectangles indicating the approximate locations of images shown in B-I. **(B)** Confocal image of GFP^{+} neurons (green) in the ACB and around the aco counterstained with DAPI (blue). **(C)** Zoom of the image in the white square in B. **(D)** Confocal image of GFP^{+} and RFP^{+} neurons and astrocytes (bushy cells) in cortical layer II. **(E)** GFP^{+} (black) neurons in cortical layer II. **(F)** Confocal image and projections of a GFP^{+} cortical layer II cell that immunostained positive for NeuN (red). **(G)** Confocal image of GFP^{+} neuron in the deep layer of the cortex. **(H)** Zoom of the neuron in the white square in G. **(I)** Confocal image of GFP^{+} neuron in the deep layer of the cortex. Inset: GFP fluorescence overlaid with DIC to illustrate the location of the corpus callosum. CC: corpus callosum; CP: caudate putamen; ACB: accumbens nucleus; aco: anterior commissure. Scale bars: 140 µm (B) 70 µm (C), 80 µm (D and G), 40 µm (E, F, and I), 30 µm (H).

Identification of Hif1 as a survival cue to newborn neurons and a determinant of dendritic growth

To examine Hif1a mRNA level, we performed endpoint RT-PCR from cDNA generated from CRE-electroporated (ipsilateral) and contralateral olfactory bulb (OB) of P21 *Tsc1*$^{\text{fl/mut}}$/R26R mice. Five sets of primers were designed to amplify Hif1a mRNA transcripts using RT-PCR. Two of the five primers amplified the predicted size product with no genomic DNA contamination or primer dimers (**Fig. 7A**) and displayed single peak melt curves (data not shown). Both primer sets demonstrated increases in Hif1a transcripts in the OB containing *Tsc1*$^{\text{null}}$ neurons. To better quantify the increases, we performed quantitative (q) RT-PCR using the standard curve method with the most sensitive Hif1a primer set and GAPDH primer for normalization. There was a 3-fold increase in the Hif1a transcript levels in the OB containing *Tsc1*$^{\text{null}}$ neurons compared to the contralateral OB (**Fig. 7B**, N=6 mice for each condition, $p<0.05$). This increase is likely underestimated because of the low percentage of RFP$^+$ neurons in the OB.

Hif1a forms a heterodimer with ARNT and regulates transcriptional activity of genes containing HIF response elements (HRE) within the promoter. We thus examined whether Hif1a-dependent gene transcription was increased in the OB containing *Tsc1*$^{\text{null}}$ neurons. We performed *in vivo* gene reporter assays by co-electroporating plasmids encoding CRE, a constitutively active renilla luciferase, or photinus pyralis luciferase under the control of HRE in *Tsc1*$^{\text{fl/mut}}$/R26R and *Tsc1*$^{\text{fl/wt}}$/R26R mice (**Fig. 7C**). The HRE-luciferase gene reporter activity was significantly increased in P28 OB containing *Tsc1*$^{\text{null}}$ neurons compared to OB containing *Tsc1*$^{\text{het}}$ neurons (**Fig. 7D**, n=18, $p<0.001$, mean= 3.1 vs. 0.4). Collectively, these experiments show that *Tsc1* deletion in newborn neurons is sufficient to increase Hif1a levels and induce transcriptional transactivation.

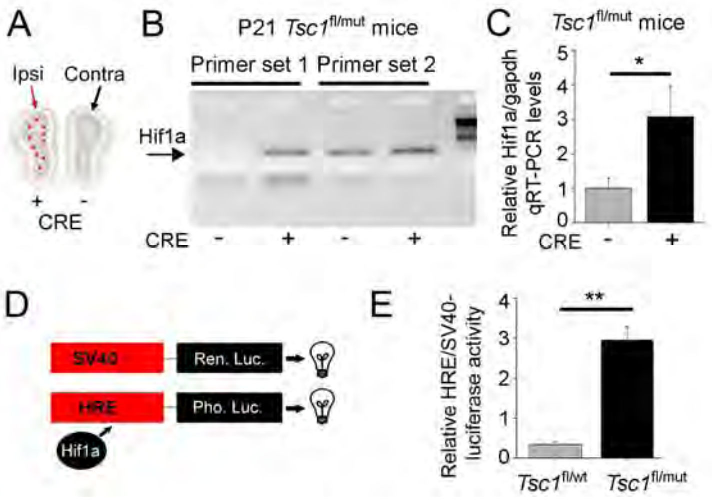

Figure 7: Hif1a mRNA and activity are up-regulated in newborn *Tsc1*$^{\text{null}}$ neurons. (A) Diagram of coronal OB sections. The ipsilateral section contains GFP$^+$/RFP$^+$ cells that contained CRE following electroporation at P1 in the SVZ. **(B)** PCR gels of Hif1a cDNA obtained from ipsilateral (CRE+) and contralateral (CRE-) P21 *Tsc1*$^{\textit{fl/mut}}$ /R26R OB using two primer sets. **(C)** Bar graphs of the relative abundance of Hif1a mRNA measured by qRT-PCR and obtained from ipsilateral (CRE+) and contralateral OB from P28 *Tsc1*$^{\textit{fl/mut}}$/R26R mouse. **(D)** Diagram of the luciferase vectors. **(E)** Bar graphs of the relative luciferase activity due to Hi1fa increase in CRE-containing OB from P28 *Tsc1*$^{\text{fl/wt}}$ and *Tsc1*$^{\text{fl/mut}}$ mice. *: $p<0.05$; **: $p<0.01$.

To determine the function of supraphysiological levels of Hif1a, we performed postnatal electroporations of a Hif1a overexpression vector in SVZ cells of *Tsc1*$^{wt/mut}$ mice. For control, a GFP-encoding vector was electroporated. When these vectors were co-electroporated with HRE or constitutively active luciferase gene reporters, we found that Hif1a overexpression produced a significant 4-fold increase in HRE transcriptional activation in P28 OB compared to GFP expression ($p<0.001$, n=11 and 6, respectively, **Fig. 8A**). Hif1a overexpression produced no obvious migratory defects (data not shown). Since *Tsc1* knockout has been reported to enhance dendrite complexity in the OB and cortex, we performed sholl analysis of Hif1a- or GFP-expressing granule cell dendrites in P28 coronal OB sections. Hif1a overexpression induced a significant increase in basal dendrite complexity and length (n=23, N=3 for Hif1a and n=30, N=3, for GFP, **Fig. 8C-E**). Thus, Hif1a overexpression in *Tsc1*^{het} neurons is sufficient to induce transcriptional transactivation and increase the dendritic complexity of these newborn neurons.

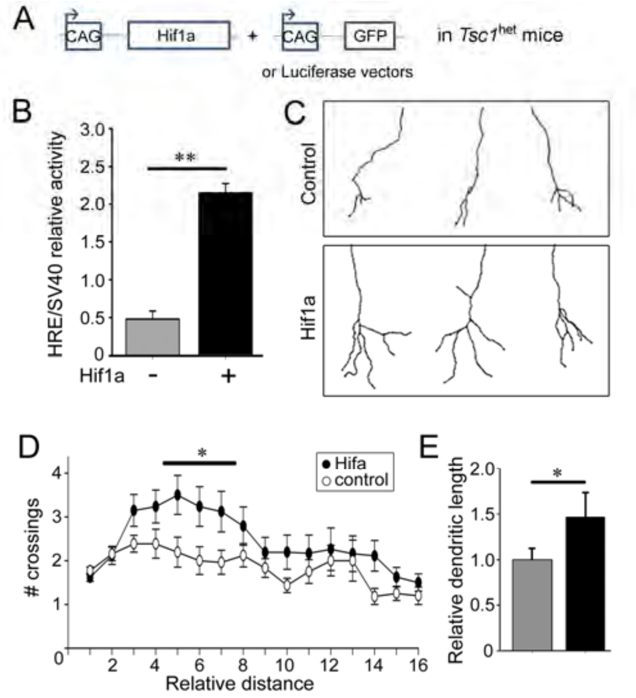

Figure 8: Hif1a overexpression increases the dendritic complexity of newborn neurons. (A) Diagram of the vectors used in *Tsc1*$^{wt/mut}$ mice. **(B)** Bar graphs of the relative luciferase activity induced by Hi1fa overexpression in OB from P28 *Tsc1*$^{wt/mut}$ mice. **(C)** Representative examples of traced basal dendrites from GFP (control)- or Hif1a-overexprressing granule cells. **(D)** Number (#) of crossings as a function of the relative distance from traced control (while) and Hif1a-overexpressing (black) granule cells. **(E)** Bar graphs of the basal dendritic length in control and Hif1a-overexpressing cells. *: $p<0.05$; **: $p<0.01$.

To assess Hif1 function, we next performed Hif1a loss-of-function experiments by electroporating vectors encoding shRNA targeting Hif1a (shHif1a) or a dominant negative form of Hif1a (dnHif1a). These vectors or control vectors were co-electroporated with CRE- and GFP-encoding plasmids into *Tsc1*$^{fl/mut}$/R26R mice (**Fig. 9A**). Following electroporation of either one or two shHif1a-encoding vectors, we found an absence of GFP fluorescence in the OB upon whole brain examination at P19 and P28 (**Fig. 9B** for P19). Closer examination of OB coronal sections revealed a drastic reduction in the number of GFP^{+} shHif1a-expressing *Tsc1*^{null} neurons per section compared to control (0-5 instead of >500 cells in control, N=16 at P28 and N=6 at P19, **Fig. 9C and D**). In the SVZ of the same mice, electroporated GFP^{+} cells persisted along the lateral ventricle (**Fig. 9E**). This latter result suggests that Hif1a had no effect on SVZ cell survival in agreement with the low levels of Hif1a immunostaining in the postnatal SVZ (data not shown). Electroporation of the dnHif1a also significantly reduced the number of *Tsc1*^{null}

neurons in the OB compared to control (P17, $p<0.001$, N=11 and N=11, **Fig. 9F**) without an obvious change in the SVZ GFP^+ cell density (data not shown). These data suggest that Hif1a is required in a cell-specific manner for survival of newborn *Tsc1*^{null} neurons.

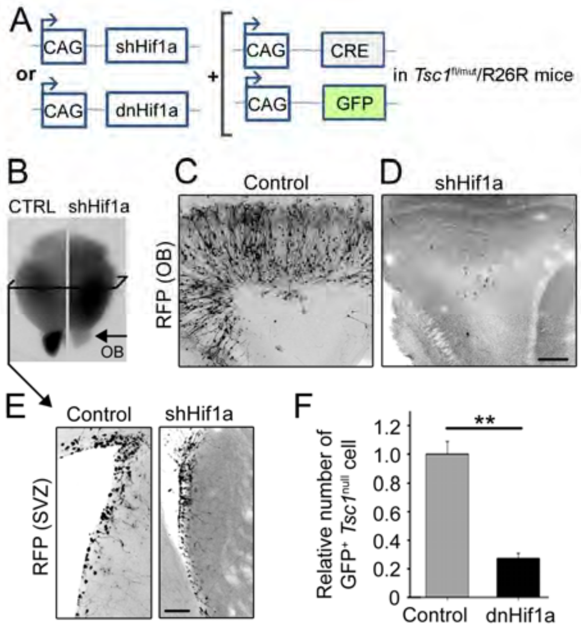

Figure 9: Hif1a is essential for the survival of newborn *Tsc1*^{null} neurons. (A) Diagram of the vectors used in *Tsc1*$^{fl/mut}$/R26R mice. **(B)** Images of P19 brain hemispheres from control or shHif1a electroporated mice. **(C and D)** Confocal images of coronal P19 OB sections containing *Tsc1*^{null} cells expressing a control (C) or Hif1a shRNA (shHif1a) (D). shHif1a eliminated *Tsc1*^{null} neurons. **(E)** Confocal images of SVZ containing *Tsc1*^{null} cells expressing a control shRNA or shHif1a. Same mice as in (C and D). **(F)** Bar graphs of the relative number of *Tsc1*^{null} cells containing a control vector (grey) or dominant negative Hif1a (black). $P<0.01$.

<u>Our ongoing work to be pursued during the next funding cycle is to:</u>

(1) Analyzing cortical excitability of the tuber and peri-tuberal cells. Our preliminary data suggest that enlarged, dysplastic tuber neurons are synaptically integrated. They receive functional synaptic inputs and generate spikes as measured using whole cell patch clamp recordings (data not shown).
(2) To identify additional molecules whose expression is altered in *Tsc1*^{null} neurons in the lesions and contribute to lesion formation..

Key Research Accomplishments

- generation of subependymal nodules and migratory heterotopia in olfactory structures

- identification of olfactory circuit abnormalities following *Tsc1* removal in neonatal neuroal progenitor cells; these defects include hypertrophic dendritic tress, ectopic neuronal location, and micronodule formation.

- identification of Hif1 as a survival factor for newborn neurons including Tsc1null neurons.

- novel findings showing that Hif1 overexpression leads to hypertrophic dendrites

- ongoing analysis of the biophysical properties of cells in and surrounding cortical tubers

Reportable Outcomes

Peer-Reviewed Manuscripts

Our new findings have recently been published in Human Molecular Genetics (Impact factor: 7.636). In addition, we have two other articles to revise, one for Human Molecular Genetics and one Journal of Neuroscience. Since last year, a commentary was also published in Epilepsy Currents on our JCI paper. We have also been asked to write a review for Trends in Neuroscience regarding adult and neonatal neurogenesis that includes a discussion on our recent findings in neonates after Tsc1 removal..

Recent publications

Feliciano DM, Quon JL, Su T, Taylor MM, Bordey A. Postnatal neurogenesis generates heterotopias, olfactory micronodules and cortical infiltration following single-cell Tsc1 deletion. *Human Molecular Genetics* (2012) 21:799-810.

Feliciano DM, Zhang S, Quon JL, and Bordey A. Hypoxia-inducible factor 1a is a Tsc1-regulated survival factor in newborn diseased neurons. Under revision for Human Molecular Genetics.

Feliciano DM and **Bordey A**. Neurons in a haystack: Evidence of Postnatal Cortical Neurogenesis. Under minor revision for Trends in Neuroscience.

Recent comment regarding our JCI paper from Dr. Wong:

Wong M. A Tuber-ful Animal Model of Tuberous Sclerosis At Last? Epilepsy Curr. (2012) 12:15-6.

Previous publications:

Feliciano D, Bordey A. Mouse model of tuberous sclerosis complex. *Medicine et Science (Paris)* (2011) 27:383-330.

Feliciano D, Su T, Lopez J, Platel JC, and **Bordey A**. Single-cell *Tsc1* knockout during murine corticogenesis generates tuber-like lesions and reduces seizure threshold without astrogliosis. *Journal of Clinical Investigation* (2011) 121:1596-1607.

Abstracts for the 2011-2012 funding cycle

Torres-Reveron J and Bordey A. Autism and Epilepsy. Yale Epilepsy Retreat (2011).

Lafourcade C, Lin T, Bordey A. Alterations on synaptic circuits by disruption of the mTOR pathway. **The summit on Drug Discovery in TS and Related disorders** (2011).

Feliciano, DM, Quon, J, Su, T, Bordey A. Focal Postnatal Tsc1 recombination in the Subventricular Zone induces mTOR pathway activation, reduces neuroblast migration rates, and generates ectopically localized neurons. **The summit on Drug Discovery in TS and Related disorders** (2011).

Feliciano, DM. Investigators' Workshop: What's Next? A Young Investigator Workshop

Title: Focal Models of Tuberous Sclerosis Complex. American Epilepsy meeting, Baltimore (2011).

Lafourcade C, Lin T, Bordey A. Alterations on synaptic circuits by disruption of the mTOR pathway. **Society of Neuroscience** (2012).

Feliciano D, Quon J, Zhang L, Bordey A. Identification of Hif1a functions in a mouse model of tuberous sclerosis complex. **Cold Spring Harbor meeting** on PTEN pathway and targets (2012).

Transgenic mice

Several mouse lines have been crossed to generate a new mouse line. This line has been published and is available to other researchers at Yale and other institutions.

The crossed lines consist of:

Rosa26R-tdTomato reporter mouse x *Tsc1*$^{fl/fl}$ x *Tsc1*$^{wt/mut}$
Rosa26R-tdTomato reporter mouse x *Tsc1*$^{fl/fl}$ x *nestin*-CreERT2

The Rosa26R-tdTomato and *Tsc1*$^{fl/fl}$ mice were purchased from Jackson Laboratories.
The *Tsc1*$^{wt/mut}$ mice were obtained from the National Cancer Institute.
Nestin-CreERT2 mice were obtained from Dr. Amelia Eisch.

Conclusions

In conclusion, we showed that focal *Tsc1* knockout in neonatal SVZ stem cells results in mTOR pathway activation and migratory alterations characterized by SEGA, heterotopia along the migratory path, olfactory bulb disorganization, and neuronal misrouting to cortical and subcortical structures. In addition, newborn *Tsc1*^{null} neurons displayed an enhanced dendritic tree. The consequences of these abnormalities on network function remains to be examined. Anyhow, we propose that neurogenesis along the SVZ progressively contributes to alterations in the forebrain during the neonatal and juvenile period resulting in progressive circuit disruption and perhaps neuropsychiatric instability in patients with TSC and other cortical malformations.

In addition, our data show for the first time that Hif1a acts as a molecular determinant of newborn neuron survival in the context of TSC. This finding suggests that TSC1-dependent Hif1a up-regulation gave *Tsc1*^{null} neurons a survival advantage despite their ectopic location in a novel microenvironment. We also found that increases in Hif1a expression and activity led to marked increase in the dendritic complexity and basal dendrite length of *Tsc1*^{het} neurons.

References

Curatolo P, Seri S, Verdecchia M, Bombardieri R (2001) Infantile spasms in tuberous sclerosis complex. Brain Dev 23:502-507.

DiMario FJ, Jr. (2004) Brain abnormalities in tuberous sclerosis complex. J Child Neurol 19:650-657.

Holmes GL, Stafstrom CE (2007) Tuberous sclerosis complex and epilepsy: recent developments and future challenges. Epilepsia 48:617-630.

Jansen FE, Van Huffelen AC, van Rijen PC, Leijten FS, Jennekens-Schinkel A, Gosselaar P, van Nieuwenhuizen O (2007) Epilepsy surgery in tuberous sclerosis: the Dutch experience. Seizure 16:445-453.

Jansen FE, Vincken KL, Algra A, Anbeek P, Braams O, Nellist M, Zonnenberg BA, Jennekens-Schinkel A, van den OA, Halley D, Van Huffelen AC, van Nieuwenhuizen O (2008) Cognitive impairment in tuberous sclerosis complex is a multifactorial condition. Neurology 70:916-923.

Jensen FE (2009) Introduction--epileptogenic cortical dysplasia: emerging trends in diagnosis, treatment, and pathogenesis. Epilepsia 50 Suppl 9:1-2.

Lacar B, Young SZ, Platel JC, Bordey A (2010) Imaging and recording subventricular zone progenitor cells in live tissue of postnatal mice. Front Neurosci 4.

Lagace DC, Whitman MC, Noonan MA, Ables JL, DeCarolis NA, Arguello AA, Donovan MH, Fischer SJ, Farnbauch LA, Beech RD, DiLeone RJ, Greer CA, Mandyam CD, Eisch AJ (2007) Dynamic contribution of nestin-expressing stem cells to adult neurogenesis. J Neurosci 27:12623-12629.

Levison SW, Goldman JE (1993) Both oligodendrocytes and astrocytes develop from progenitors in the subventricular zone of postnatal rat forebrain. Neuron 10:201-212.

Meikle L, Talos DM, Onda H, Pollizzi K, Rotenberg A, Sahin M, Jensen FE, Kwiatkowski DJ (2007) A mouse model of tuberous sclerosis: neuronal loss of Tsc1 causes dysplastic and ectopic neurons, reduced myelination, seizure activity, and limited survival. J Neurosci 27:5546-5558.

Misson JP, Edwards MA, Yamamoto M, Caviness VS, Jr. (1988) Identification of radial glial cells within the developing murine central nervous system: studies based upon a new immunohistochemical marker. Brain Res Dev Brain Res 44:95-108.

Mizuguchi M, Takashima S (2001) Neuropathology of tuberous sclerosis. Brain Dev 23:508-515.

Pathania M, Yan LD, Bordey A (2010) A symphony of signals conduct early and late stages of adult neurogenesis. Neuropharmacology 58:865-876.

Petreanu L, Alvarez-Buylla A (2002) Maturation and death of adult-born olfactory bulb granule neurons: role of olfaction. J Neurosci 22:6106-6113.

Platel JC, Dave KA, Gordon V, Lacar B, Rubio ME, Bordey A (2010) NMDA receptors activated by subventricular zone astrocytic glutamate are critical for neuroblast survival prior to entering a synaptic network. Neuron 65:859-872.

Shuang M, Liu J, Jia MX, Yang JZ, Wu SP, Gong XH, Ling YS, Ruan Y, Yang XL, Zhang D (2004) Family-based association study between autism and glutamate receptor 6 gene in Chinese Han trios. Am J Med Genet B Neuropsychiatr Genet 131B:48-50.

Thiele EA (2004) Managing epilepsy in tuberous sclerosis complex. J Child Neurol 19:680-686.

Zhou J, Shrikhande G, Xu J, McKay RM, Burns DK, Johnson JE, Parada LF (2011) Tsc1 mutant neural stem/progenitor cells exhibit migration deficits and give rise to subependymal lesions in the lateral ventricle. Genes Dev 25:1595-1600.

Appendix

Our new findings have recently been published in Human Molecular Genetics (Impact factor: 7.636). In addition, we have two other articles to revise, one for Human Molecular Genetics and one Journal of Neuroscience. Since last year, a commentary was also published in Epilepsy Currents on our JCI paper.

Recent publications

Feliciano DM, Quon JL, Su T, Taylor MM, Bordey A. Postnatal neurogenesis generates heterotopias, olfactory micronodules and cortical infiltration following single-cell Tsc1 deletion. *Human Molecular Genetics* (2012) 21:799-810.

Feliciano DM, Zhang S, Quon JL, and Bordey A. Hypoxia-inducible factor 1a is a Tsc1-regulated survival factor in newborn diseased neurons. Under revision for H*uman Molecular Genetics*.

Comment regarding our JCI paper from Dr. Wong:

Wong M. A Tuber-ful Animal Model of Tuberous Sclerosis At Last? Epilepsy Curr. (2012) 12:15-6.

Previous publications:

Feliciano D, Su T, Lopez J, Platel JC, and **Bordey A**. Single-cell *Tsc1* knockout during murine corticogenesis generates tuber-like lesions and reduces seizure threshold without astrogliosis. *Journal of Clinical Investigation* (2011) 121:1596-1607.

Feliciano D, Bordey A. Mouse model of tuberous sclerosis complex. *Medicine et Science (Paris)* (2011) 27:383-330.

Human Molecular Genetics, 2012, Vol. 21, No. 4 **799–810**
doi:10.1093/hmg/ddr511
Advance Access published on November 7, 2011

Postnatal neurogenesis generates heterotopias, olfactory micronodules and cortical infiltration following single-cell *Tsc1* deletion

David M. Feliciano[1,2], Jennifer L. Quon[1,2], Tiffany Su[1,2], M. Morgan Taylor[1,2], and Angélique Bordey[12,*]

[1]Department of Neurosurgery and [2]Department of Cellular and Molecular Physiology, Yale University School of Medicine, New Haven, CT, USA

Received September 14, 2011; Revised and Accepted October 31, 2011

Neurological symptoms in tuberous sclerosis complex (TSC) and associated brain lesions are thought to arise from abnormal embryonic neurogenesis due to inherited mutations in *Tsc1* or *Tsc2*. Neurogenesis persists postnatally in the human subventricular zone (SVZ) where slow-growing tumors containing *Tsc*-mutant cells are generated in TSC patients. However, whether *Tsc*-mutant neurons from the postnatal SVZ contribute to brain lesions and abnormal circuit remodeling in forebrain structures remain unexplored. Here, we report the formation of olfactory lesions following conditional genetic *Tsc1* deletion in the postnatal SVZ using transgenic mice or targeted single-cell electroporation. These lesions include migratory heterotopias and olfactory micronodules containing neurons with a hypertrophic dendritic tree. Most significantly, our data identify migrating glial and neuronal precursors that are re-routed and infiltrate forebrain structures (e.g. cortex) and become glia and neurons. These data show that *Tsc1*-mutant cells from the neonatal and juvenile SVZ generate brain lesions and structural abnormalities, which would not be visible using conventional non-invasive imaging. These findings also raise the hypothesis that micronodules and the persistent infiltration of cells to forebrain structures may contribute to network malfunction leading to progressive neuropsychiatric symptoms in TSC.

INTRODUCTION

Tuberous sclerosis complex (TSC) is an autosomal dominant disorder that is associated with lesions in many different organs including in the kidney, skin, heart and brain. The incidence of TSC is estimated between 1:6000 and 1:10 000 individuals (1). TSC is caused by inactivating mutations in one of two tumor suppressor genes, *TSC1* and *TSC2*, which encode hamartin and tuberin, respectively, and lead to hyperactivity of the mammalian target of rapamycin (mTOR) (2). Although TSC affects many organ systems, the neurological symptoms (e.g. seizures, autism, psychiatric problems) cause the most significant disability and morbidity (3–6).

Neurological symptoms in TSC result from anomalies in brain development, in particular cortical neurogenesis, leading to an abnormal circuitry and the formation of brain lesions (7–16). These lesions are thought to occur *in utero* when cortical neurons are generated and migrate to their final location (8). Indeed, cortical lesions have been detected as early as 19 weeks of gestation in humans (17) and were generated following *Tsc1* deletion in embryonic neural progenitor cells and developing neurons (9). Neurogenesis, however, does not stop at birth, but persists in selective regions of the neonatal and adult brain in all species examined, including humans (18–21). This continual generation of new neurons confers plasticity at the cellular and circuit levels. It also raises the possibility that postnatal neurogenesis in individuals with TSC could contribute to specific brain lesions and abnormal circuit remodeling (7,22).

The subventricular zone (SVZ) along the lateral ventricle and the hippocampal subgranular zone of the dentate gyrus are sites of active neurogenesis throughout life (21,23). The SVZ contains the largest pool of neural progenitor cells in

---

[*]To whom correspondence should be addressed at: Yale Univ. Sch. Med., 333 Cedar St, FMB 422. New Haven, CT 06520-8082, USA. Tel: +1 2037372515; Fax: +1 2037372159; Email: angelique.bordey@yale.edu

the adult human brain and span the entire cerebrum (19,24–26). During the neonatal period, the SVZ generates both neurons and glia, and essentially neurons in adults (27). Newborn neuroblasts migrate to the olfactory bulb where they differentiate into interneurons (19,20,28). A subset of these neurons also migrates to cortical and subcortical structures most prominently during the neonatal period (29–31). Individuals with TSC display lesions (referred to as nodules or hamartomas) in the forebrain, such as the olfactory and basal ganglia structures (32–38). In addition, they display SVZ nodules and giant cell subependymal astrocytomas (SEGAs) that have been recently generated in mice by deleting *Tsc1* in neonatal neural progenitor cells (39–41). Collectively, these pieces of evidence suggest that *Tsc1*$^{\mathrm{null}}$ neurons are continuously generated from the postnatal SVZ, but their contribution to olfactory lesions and alterations in surrounding neuronal circuits remain unexplored.

Using genetic tools including conditional transgenic mice and single-cell genetic targeting, we report that olfactory lesions (i.e. heterotopic and micronodules) are generated from the postnatal SVZ. In addition, we found a continual infiltration of cells, including neurons and glia, from the migratory stream to cortical and subcortical areas. This finding raises new questions regarding the contribution of micronodules and ectopic migration to progressive circuit disruptions during neonatal and perhaps adult life in patients with TSC and other genetic disorders associated with cortical malformation.

RESULTS

Neonatal *Tsc1* deletion using nestin-CreER$^{\mathrm{T2}}$ mice leads to olfactory lesions and the presence of enlarged neurons in the cortex

To examine whether postnatal neurogenesis contributes to olfactory lesions, we used conditional transgenic mice as recently reported to induce SVZ nodules and SEGA (41). Loss of heterozygosity in SVZ cells was achieved using mice expressing *Tsc1* alleles flanked by LoxP sites (floxed, fl) crossed with nestin-CreER$^{\mathrm{T2}}$/R26R-YFP mice to generate *Tsc1*$^{\mathrm{fl/fl}}$/nestin$^{\mathrm{CreERT2}}$ mice (Fig. 1A) (12,42). These nestin-CreER$^{\mathrm{T2}}$ mice have been used to induce selective recombination in cells of the neurogenic zones in adults (43). In neonates, nestin is also expressed in astrocytes and progressively disappears as they mature and acquire glial fibrillary acidic protein (GFAP) in rodents. Upon tamoxifen injection in *Tsc1*$^{\mathrm{fl/fl}}$/nestin$^{\mathrm{CreERT2}}$, nestin-expressing cells, including SVZ cells and astrocytes, are expected to lose *Tsc1* and express YFP. Control mice were *Tsc1*$^{\mathrm{fl/wt}}$/nestin$^{\mathrm{CreERT2}}$ (wild-type, wt).

Tamoxifen was injected at P7 (two injections) and brains were collected at postnatal day (P) 28. To examine whether recombination at the *Tsc1* allele occurred, we prepared genomic DNA from the P28 cortex from *Tsc1*$^{\mathrm{fl/fl}}$/nestin$^{\mathrm{CreERT2}}$ mice. We detected a *Tsc1*-mutant allele band, suggesting successful recombination ($n = 3$, Fig. 1B). In addition, as recently reported, *Tsc1*$^{\mathrm{fl/fl}}$/nestin$^{\mathrm{CreERT2}}$ mice displayed GFAP- and RC2-rich SEGA-like lesions in the ventral SVZ (Fig. 1D, GFAP not shown, locations shown on the diagram in Fig. 1C) (41). RC2 is a radial glial cell marker (44).

Every *Tsc1*$^{\mathrm{fl/fl}}$/nestin$^{\mathrm{CreERT2}}$ mouse displayed small YFP^{+} lesions along the migratory tract taken by newborn neurons to reach the olfactory bulb, the rostral migratory stream (RMS) ($n = 5$, Fig. 1C and E, red circle). These lesions consisted in the accumulation of 5–20 YFP^{+} cells that were not observed in *Tsc1*$^{\mathrm{fl/wt}}$/nestin$^{\mathrm{CRERT2}}$ mice ($n = 3$, Fig. 1E). Strikingly, YFP^{+} cells were also visible throughout the cortex in *Tsc1*$^{\mathrm{fl/fl}}$/nestin$^{\mathrm{CRERT2}}$ mice (Fig. 1F), in the AON, and around the anterior commissure (data not shown). Closer examination of these cells revealed the presence of bushy cells with an astrocytic morphology and cells with a pyramidal neuron morphology (Fig. 1G for neurons). While YFP^{+} astrocytes were also observed in the cortex of *Tsc1*$^{\mathrm{fl/wt}}$/nestin$^{\mathrm{CreERT2}}$ mice, YFP^{+} neurons were rarely detected (1–2 per section, data not shown).

These data suggest that lesions in the olfactory migratory tract can form postnatally. In addition, ectopic neurons were found in the cortex of *Tsc1*$^{\mathrm{fl/fl}}$ mice. To identify whether cells in the lesions and the cortex were generated in the SVZ, we used an alternative approach, neonatal electroporation. This method also allows genetic manipulations of a small group of cells as opposed to global modification using transgenic mice. In addition, we used mice expressing an fl and a mutant *Tsc1* allele (*Tsc1*$^{\mathrm{fl/mut}}$) because individuals with TSC inherit a viable and a mutant *Tsc1* (or *Tsc2*) allele. *Tsc1*$^{\mathrm{fl/wt}}$ mice (wt for wild-type) were control littermates.

Targeted *Tsc1* removal and mTOR activation in newborn neurons via neonatal electroporation

Neonatal electroporation allows precise targeting of plasmids into neural progenitor cells lining the lateral ventricle (45). These progenitor cells generate neurons that migrate to the olfactory bulb via the RMS and are synaptically mature by 3–4 weeks after birth (46). We used *Tsc1* mice crossed with R26R-Stop-RFP mice (RFP, red fluorescent protein). In *Tsc1*$^{\mathrm{fl/mut}}$/RFP mice, Cre recombinase (Cre) expression is expected to lead to TSC1 loss and RFP expression (Fig. 2A). RFP^{+} neurons are thus expected to be *Tsc1*$^{\mathrm{null}}$ while surrounding RFP^{-} neurons are *Tsc1*$^{\mathrm{haplo}}$ (haplo for haploinsufficient).

Cre- and GFP-encoding plasmid were electroporated into SVZ progenitor cells at P0–1 resulting in visible GFP fluorescence 1-day post-electroporation (Fig. 2B and C) (45,47). GFP allows to birth-mark neurons born during the first 7–10 days post-electroporation because GFP is diluted as cells divide while RFP is permanently expressed (45) (Fig. 2D). As a result, RFP^{+} but not GFP^{+} newborn neurons continuously accumulate in the circuit (Fig. 2E). To test for recombination at the *Tsc1* allele, we prepared genomic DNA from P7 ipsilateral (i.e. containing RFP^{+} cells) and contralateral olfactory bulbs from *Tsc1*$^{\mathrm{fl/fl}}$/RFP mice. A *Tsc1* mutant allele band was detected only in the ipsilateral olfactory bulb, suggesting that *Tsc1* was removed in RFP^{+} cells ($n = 3$, Fig. 2F). Next, we performed reverse transcription polymerase chain reaction (RT-PCR) for *Tsc1* and western blot analysis from P28 olfactory bulb (OB) when *Tsc1*$^{\mathrm{null}}$ neurons have accumulated in the OB

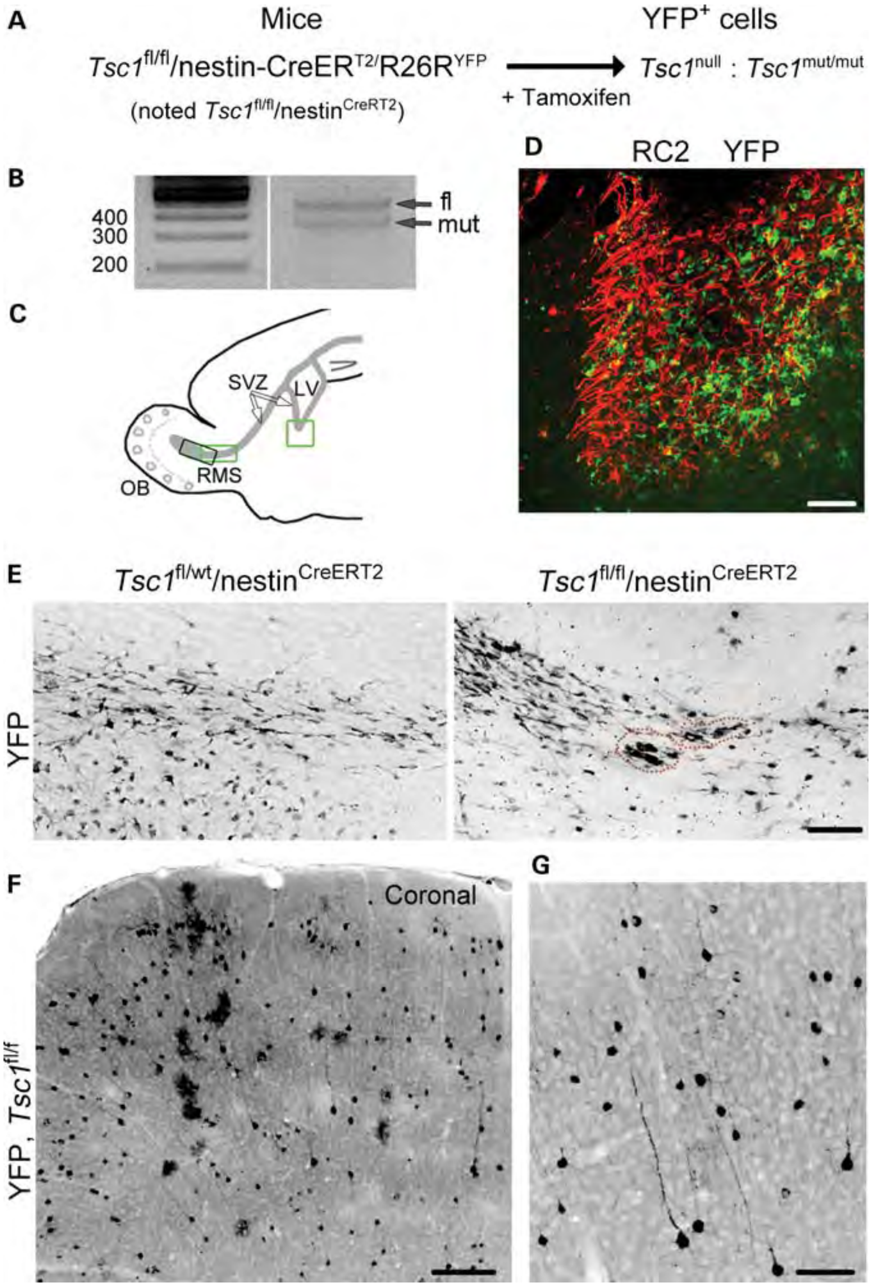

Figure 1. Postnatal deletion of *Tsc1* using inducible transgenic mice. (**A**) The diagram illustrating the inducible transgenic mouse line used to delete *Tsc1* (i.e. null) and express YFP in nestin-expressing cells and their progeny following tamoxifen injection at P7. (**B**) PCR gels from genomic DNA obtained from a P28 olfactory bulb following tamoxifen at P7. A mutant band in addition to the fl band is visible. (**C**) The diagram illustrating the locations of the images shown in (**D**) (ventral SVZ, green square) and in (**E**) (RMS, green square, for *Tsc1*$^{\mathrm{fl/fl}}$ and black square for *Tsc1*$^{\mathrm{fl/wt}}$) on a sagittal section. LV, lateral ventricle; SVZ, subventricular zone; OB, olfactory bulb; RMS, rostral migratory stream. (D) The P28 image of the RC2 (red)-rich SVZ nodule containing YFP^{+} *Tsc1*$^{\mathrm{null}}$ cells following tamoxifen-induced recombination at P7. (E) Confocal images of YFP-immunopositive cells in the RMS/RMS-OB of *Tsc1*$^{\mathrm{fl/wt}}$/nestin$^{\mathrm{CreERT2}}$ and RMS of *Tsc1*$^{\mathrm{fl/fl}}$/nestin$^{\mathrm{CreERT2}}$ following tamoxifen injections at P7. The dotted orange lines highlight small clusters of misplaced cells in the RMS. (**F** and **G**) Confocal images of YFP^{+} cells (low and high magnifications) in the cortex of *Tsc1*$^{\mathrm{fl/fl}}$/nestin$^{\mathrm{CreERT2}}$ mice. Scale bars: 70 µm (D, E and G) and 200 µm (F).

for over 3 weeks, which increase our chance to detect changes in mRNA and protein levels. End-point and quantitative RT–PCR for *Tsc1* illustrated that there was a 30–40% decrease in *Tsc1* mRNA in the ipsilateral versus the contralateral *Tsc1*$^{\mathrm{fl/mut}}$ olfactory bulb ($n = 3$, P28, Fig. 2G). Western blot illustrates a decrease in TSC1 (hamartin) expression in *Tsc1*$^{\mathrm{fl/mut}}$ compared with *Tsc1*$^{\mathrm{fl/wt}}$ ipsilateral olfactory bulbs (Fig. 2H).

mTOR hyperactivity results in elevated phosphorylation of ribosomal protein S6 (pS6) and 4E-BP. We immunostained for pS6 (Ser 240/244) in P28 olfactory bulb sections. In *Tsc1*$^{\mathrm{fl/mut}}$ mice, RFP^{+} neurons displayed a significant 115% increase in pS6 staining intensity compared with surrounding RFP^{-} neurons ($P < 0.001$, Fig. 3A–D). In contrast, 4E-BP phosphorylation was not altered (data not shown). There was

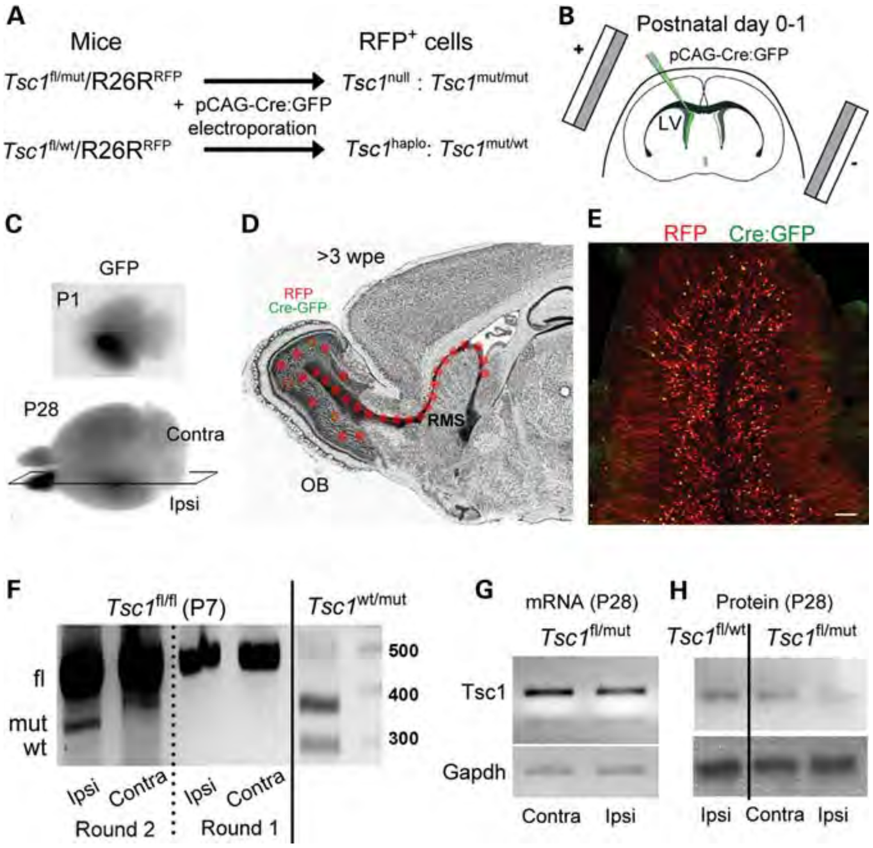

Figure 2. Postnatal deletion of *Tsc1* using neonatal electroporation and the Cre-Lox system. (**A**) Schematic describing the loss of one or two *Tsc1* alleles in cells containing a plasmid encoding Cre:GFP under the CAG promoter that is expressed through neonatal electroporation in *Tsc1*$^{\text{fl/wt}}$/R26R and *Tsc1*$^{\text{fl/mut}}$/R26R, respectively. Cells containing the pCAG-Cre:GFP also express RFP. (**B**) The diagram illustrating the principle of neonatal electroporation of a plasmid into neural progenitor cells lining the lateral ventricle. (**C**) Images of P1- and P28 fixed brains containing RFP$^+$ cells in the ipsilateral olfactory bulb. (**D**) The diagram illustrating the migratory path and the final location of newly born cells 3 weeks post-electroporation (wpe). RFP expression persists permanently due to its genomic integration (R26R mice), while GFP expression from either a pCAG-GFP or pCAG-Cre:GFP is diluted in newly born cells due to successive cell division. As a result, only cells born during the first 7–10 days express GFP. (**E**) The confocal image of RFP$^+$ and GFP$^+$ newly born cells in a coronal olfactory bulb section. RFP$^+$/GFP$^+$ cells outnumber RFP$^+$/GFP$^-$ cells. Scale bar: 70 µm. (**F**) PCR gels from genomic DNA obtained from the ipsilateral (mRFP-containing cells) and contralateral olfactory bulb from P7 *Tsc1*$^{\text{fl/fl}}$/R26R and *Tsc1*$^{\text{wt/mut}}$/R26R mice electroporated at P1. (**G**) PCR gels of Tsc1 and Gapdh cDNA obtained from the ipsilateral and contralateral P28 *Tsc1*$^{\text{fl/mut}}$/R26R olfactory bulb. All the gels were run on the same blots. (**H**) Western blots of TSC1 (hamartin) and GAPDH obtained from ipsilateral P28 *Tsc1*$^{\text{fl/wt}}$/R26R and *Tsc1*$^{\text{fl/mut}}$/R26R olfactory bulbs.

no difference in pS6 staining intensity in RFP$^+$ compared with RFP$^-$ neurons from *Tsc1*$^{\text{fl/wt}}$ mice (data not shown). Another well-known consequence of mTOR hyperactivity is an increase in cell size that was visible in *Tsc1*$^{\text{null}}$ neurons (Fig. 3C). RFP and 4′,6-diamidino-2-phenylindole (DAPI) counterstain were used to quantify soma and nuclei size in *Tsc1*$^{\text{fl/mut}}$ mice (Fig. 3E and F). RFP$^+$ *Tsc1*$^{\text{null}}$ neurons were ~3 times larger than RFP$^-$ neurons and their nuclei 55% larger ($P < 0.001$, Fig. 3G).

Collectively, neonatal electroporation is an effective method to induce *Tsc1* deletion in newborn neurons leading to mTOR pathway activation and cytomegally.

Tsc1$^{\text{null}}$ cells form the migratory heterotopia in and out of the RMS

Gross examination of sagittal sections from P28 *Tsc1*$^{\text{fl/mut}}$ mice revealed the presence of the migratory heterotopia, defined by the ectopic location or misplacement of groups of *Tsc1*$^{\text{null}}$ cells. Examination of sagittal sections at low magnification led us identification of the heterotopia in all animals examined ($n = 13$) that were found at three major locations: in the RMS both at its entry point caudally and at the interface RMS and RMS-OB, in the RMS-OB and adjacent to the RMS in the AON as well as near the anterior commissure olfactory limb (Fig. 4A and B, black rectangles indicate the location of the heterotopia). No migratory heterotopias were visible in electroporated *Tsc1*$^{\text{fl/wt}}$/R26R mice (data not shown).

Closer examination of the heterotopia revealed two categories, some with an apparent mixed neuroglial phenotype (Fig. 4C–G) and some with a neuronal phenotype (Fig. 4H and I). The mixed neuroglial phenotype was visible due to the presence of a meshwork of lamelipodia-like processes giving a nodular appearance or the presence of cells with neuronal or glial morphology (Fig. 4C). Heterotopia with a lamelipodia-like structure was preferentially found in the AON as shown in Figure 4B and C. Heterotopia in the RMS and RMS-OB displayed cells with an astrocytic (bushy), a neuronal morphology or an undifferentiated morphology

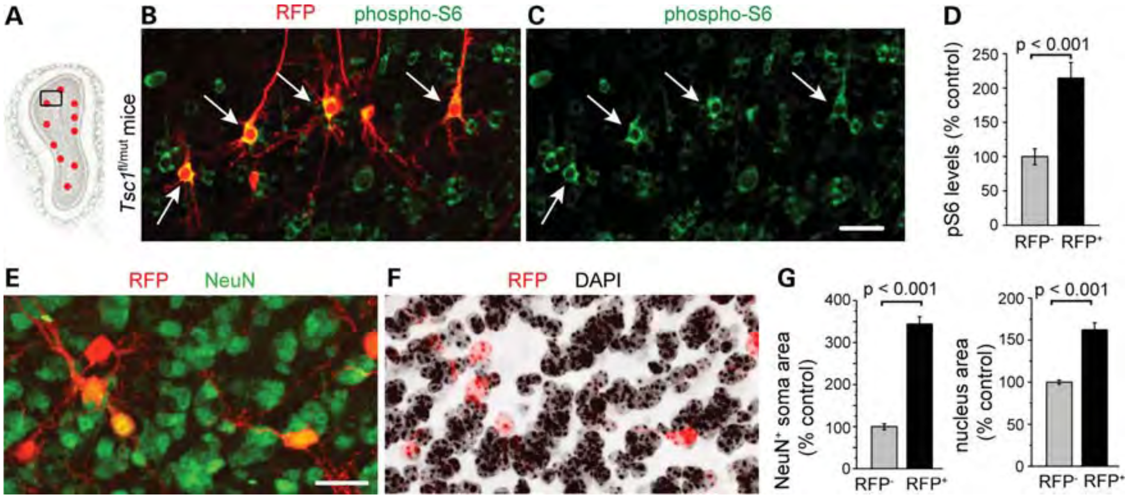

Figure 3. *Tsc1* knockout hyper-activates the mTOR pathway and leads to cytomegaly. (**A**) The diagram of a coronal olfactory bulb section with the black square indicating the approximate location of the image in (**B**) and (**C**). (B and C) Confocal images of RFP fluorescence (red) and phospho-S6 immunostaining (green). Arrows point to neurons with an enlarged pS6 soma. (**D**) The bar graph of the pS6 intensity of all RFP^{+} neurons as a % of control RFP^{-} neurons (mean ± SEM, *t*-test). (**E** and **F**) Confocal images of RFP fluorescence (red) and NeuN immunostaining (green, E) and DAPI counterstain (black, F). (**G**) Bar graphs of the NeuN^{+} soma area and the nuclear area as a % of control. Scale bars: 30 µm (B and C) and 20 µm (E and F).

(Fig. 4D–G). Some cells stained for the astrocytic marker GFAP (data not shown). Cells with a neuronal morphology displayed extensive dendrites with spines and a thin process identified as an axon by the presence of varicosities (white arrows, Fig. 4E–G). Cells forming the heterotopia displayed enlarged cells body compared with surrounding cells, in particular doublecortin (DCX)-immunopositive neuroblasts in the RMS (Fig. 4F and G, DCX staining not shown).

Mixed phenotype–heterotopia comprised GFP^{+} and GFP^{-}/RFP^{+} cells. In wt mice, GFP^{+} cells, which are born between P0 and P10, should have reached the olfactory bulb by P28 (see 45 for more details). Indeed in *Tsc1*$^{\mathrm{fl/wt}}$/R26R mice, only 8% of the RFP^{+} cells were GFP^{+} in the RMS (23/250 cells, $n = 3$ mice). In contrast, we found that 22% of *Tsc1*$^{\mathrm{null}}$ RFP^{+} cells were GFP^{+} cells in the RMS (280/1092 cells, $n = 3$, $P < 0.0001$, Fisher's exact test). Thus, heterotopia contained early born GFP^{+} cells that are stalled in the RMS and may thus trap late born cells as well as disrupt their migratory path.

Heterotopia comprised of 3–15 cytomegalic neurons is also visible along the RMS-OB and more specifically, in the anterior commissure olfactory limb (Fig. 4H and I). These cells displayed a neuronal morphology and were NeuN and pS6 immunopositive (data not shown). The majority of these ectopic neurons were GFP^{+} and thus early born (Fig. 4H).

Tsc1$^{\mathrm{null}}$ cells in the RMS display abnormal morphology and are slow or stalled

Outside the heterotopia, the RMS of P28 *Tsc1*$^{\mathrm{fl/mut}}$/R26R mice appeared more disorganized compared with that of *Tsc1*$^{\mathrm{fl/wt}}$/R26R mice (Fig. 5A and B). This appearance was due to the presence of cells with a more complex morphology and enlarged soma scattered along the RMS (arrows, Fig. 5B). As a mean, *Tsc1*$^{\mathrm{null}}$ cells had one more process than *Tsc1*$^{\mathrm{haplo}}$ cells (a mean of 2.2 ± 0.2 versus 1.4 ± 0.1, $P < 0.05$, Fig. 5C). Complex *Tsc1*$^{\mathrm{null}}$ cells were DCX^{-}, while morphologically simpler cells were DCX^{+} identifying them as neuroblasts (data not shown).

Next, we performed a migration assay in acute sagittal slices from the RMS of P21 mice (45,47). *Tsc1*$^{\mathrm{haplo}}$ neuroblasts migrated at a 54.4 ± 2.2 µm/h, which is similar to a previously reported value for neuroblast migration in wt mice (47–49). *Tsc1*$^{\mathrm{null}}$ neuroblasts migrated at 37.1 ± 2.5 µm/h and were thus 33% slower than *Tsc1*$^{\mathrm{haplo}}$ cells (128 and 83 cells, $P < 0.0001$, Fig. 5D). *Tsc1*$^{\mathrm{null}}$ cells with a complex morphology were stationary.

We also found scattered *Tsc1*$^{\mathrm{null}}$ giant cells characterized by a soma size 3–4 times larger than that of other *Tsc1*$^{\mathrm{null}}$ cells (Fig. 5E). These cells had a disheveled morphology, were NeuN negative and contain multiple nuclei (Fig. 5E–G). Two nuclei can be appreciated in Figure 5G and H. A mean of five giant cells were found per RMS of *Tsc1*$^{\mathrm{fl/mut}}$/R26R mice, while none was seen in the RMS of *Tsc1*$^{\mathrm{fl/wt}}$/R26R mice.

Micronodules throughout the olfactory bulb containing neurons with a hypertrophic dendritic tree

Upon entering the olfactory bulb, the majority of newborn neurons integrate in the granule cell layer. Ultimate circuit formation depends on proper cell placement and morphogenesis. We thus examined the overall organization of granule cells and their dendritic arbor. In coronal olfactory bulb sections, the overall cell distribution was disrupted in *Tsc1*$^{\mathrm{fl/mut}}$/R26R compared with *Tsc1*$^{\mathrm{fl/wt}}$/R26R mice (Fig. 6A and B). This is in addition to obvious increase in the size of *Tsc1*$^{\mathrm{null}}$ cells as measured in Figure 2. Perhaps, more visible in sagittal sections was the apparent clumping of cytomegalic *Tsc1*$^{\mathrm{null}}$ cells (Fig. 6D), while *Tsc1*$^{\mathrm{haplo}}$ cells were equally distributed (Fig. 6C). To quantify the disorganization of granule cells, we performed nearest neighbor calculations in which the

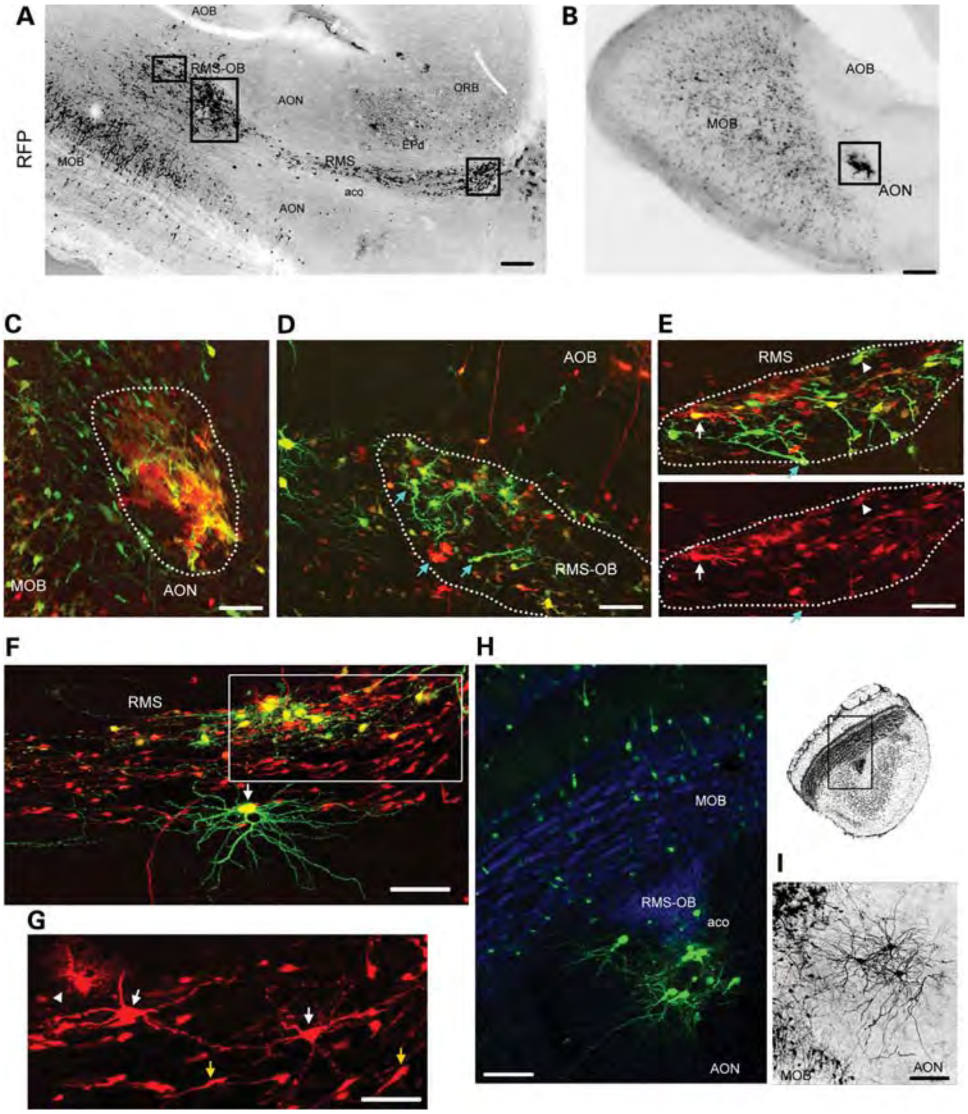

Figure 4. *Tsc1*$^{\mathrm{null}}$ cells form the migratory heterotopia in and out of the RMS. Low magnification photographs of RMS/RMS-OB (**A**) and AON (**B**) lesions containing RFP^{+} cells in sagittal sections of *Tsc1*$^{\mathrm{fl/mut}}$/R26R mice electroporated at P1 with pCAG-Cre:GFP and pCAG-GFP. The black rectangles illustrate the approximate locations of images shown in (**C**)–(**E**). (C) The confocal image of a lesion in the AON, the location of which is shown in (B). The lesion contains RFP^{+}/GFP^{+} and RFP^{+}/GFP^{-} cells. (D–**G**) Confocal Z-stack images of lesions in the RMS-OB (D) and RMS (E and F), the locations of which are shown in (A). G is a zoom and smaller Z-stack of the region in the white rectangle in F. Blue arrows (D and E) point to cells with an immature morphology. White arrows (E, F and G) point to some neurons. The arrowhead (E and G) points to examples of cells resembling astrocytes. Yellow arrows (in G) point to neuroblasts. (**H** and **I**) Confocal Z-stack images of neuronal heterotopias in the aco of the olfactory bulb in a coronal section (GFP^{+} neurons in green and DAPI in blue, H) and the neuronal heterotopia in the AON (black, I). Scale bars: 700 µm (A and B), 40 µm (C), 35 µm (D), 50 µm (E and G) and 70 µm (F, H and I). aco, anterior commissure, olfactory limb; AOB, accessory olfactory bulb; AON, accessory olfactory nucleus; aco:EP, doral endopiriform cortex; ORB, orbital cortex.

density of cells and the distance between each were measured (Fig. 6E). These measurements were compared with a theoretical Poisson distribution. The difference between the theoretical and experimental values in *Tsc1*$^{\mathrm{fl/mut}}$/R26R mice was significantly lower than that in *Tsc1*$^{\mathrm{fl/wt}}$/R26R mice ($R = 4.2 \pm 1.2$, $n = 10$ versus $R = 9.0 \pm 1.5$, $n = 12$ sections, Fig. 6F), suggesting a decreased organization in the *Tsc1*$^{\mathrm{fl/mut}}$ olfactory bulb ($P < 0.05$).

Another observation in coronal sections was the hypertrophic dendritic tree of *Tsc1*$^{\mathrm{null}}$ granule neurons (Fig. 7A). Using Scholl analysis of the proximal dendrites, we found that the number of dendritic crossings was increased in *Tsc1*$^{\mathrm{null}}$ compared with *Tsc1*$^{\mathrm{haplo}}$ neurons (Fig. 7B).

Newborn neurons are rerouted to cortical and subcortical areas

Considering that cortical neurons were observed in the *Tsc1*$^{\mathrm{fl/fl}}$/nestin$^{\mathrm{CreRT2}}$, we examined for the presence of neurons in cortical and subcortical structures in coronal sections. In all *Tsc1*$^{\mathrm{fl/mut}}$ brains examined, we found GFP^{+} neurons in the nucleus accumbens and in the cortex (Fig. 8). The majority of neurons were GFP^{+} suggesting that they were born during the neonatal period. Such neurons were absent in the Tsc1$^{\mathrm{fl/wt}}$ brain or very rare (1 per section occasionally). In the nucleus accumbens, neurons were located at the base of the lateral ventricle and around the anterior commissure

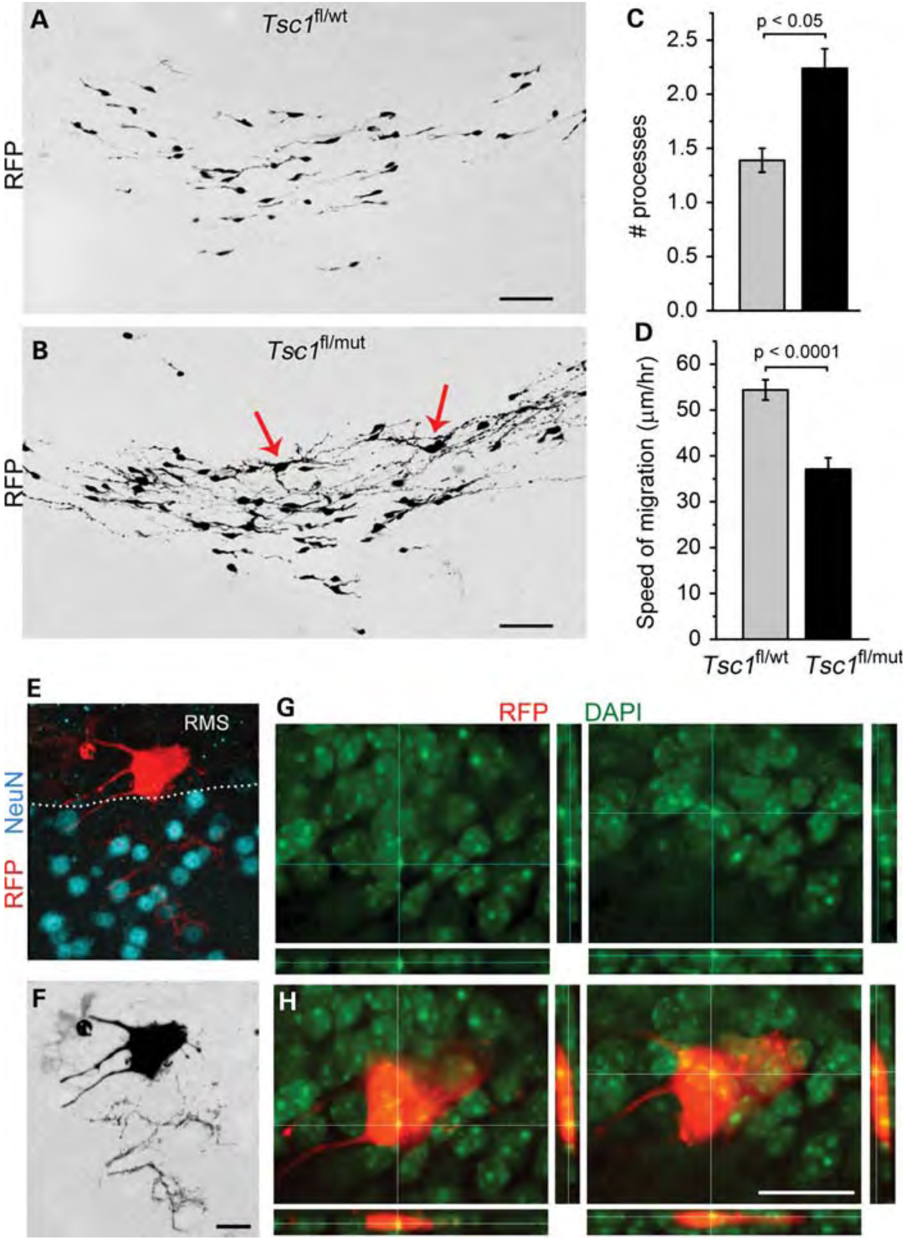

Figure 5. $Tsc1^{null}$ cells in the RMS display a hypertrophic morphology and are slow. (**A** and **B**) Confocal Z-stack images of RFP$^+$ cells in the RMS of $Tsc1^{fl/wt}$/R26R and $Tsc1^{fl/mut}$/R26R mice. Bar graphs of the number of processes (**C**) and the speed of RFP+ cell migration (**D**) in $Tsc1^{fl/wt}$/R26R (gray) and $Tsc1^{fl/mut}$/R26R (black). (**E**) The confocal image of an enlarged RFP$^+$ cells (red) and NeuN immunostaining (blue) in the RMS sending a process in the accessory olfactory nucleus. (**F**) The same cell as in (E) in black and white. (**G** and **H**) Projections from the same RFP$^+$ cell (red) as in (E) and DAPI counterstain (green, alone in G) to illustrate the presence of two nuclei. Scale bars: 50 μm (A and B), 30 μm (F) and 40 μm (G).

(Fig. 8B and C). GFP$^+$ cells were identified as neurons based on NeuN immunostaining. In the cortex, 10–15 neurons were found per sections. Neurons occurred in clusters of 2–6 and were located in the deep cortical layers and in layer II (Fig. 8D–I). Cortical neurons display an extensive dendritic tree with spines as well as a thin process with varicosities resembling an axon.

DISCUSSION

Here, we show that focal *Tsc1* knockout in the postnatal SVZ results in mTOR pathway activation and migratory alterations characterized by the heterotopia along the migratory path, olfactory bulb disorganization and neuronal misrouting to cortical and subcortical structures. In addition, newborn $Tsc1^{null}$ neurons displayed a reduced migration rate and an enhanced dendritic tree.

To explore whether postnatal neurogenesis contributed to some of the lesions observed in TSC patients, we used two strategies. First, we used inducible transgenic mice, in which tamoxifen injections led to *Tsc1* loss in nestin-expressing cells, including SVZ cells. This resulted in the formation of SEGA-like lesions as reported recently (41). In addition, we found small heterotopias (i.e. clusters of misplaced cells)

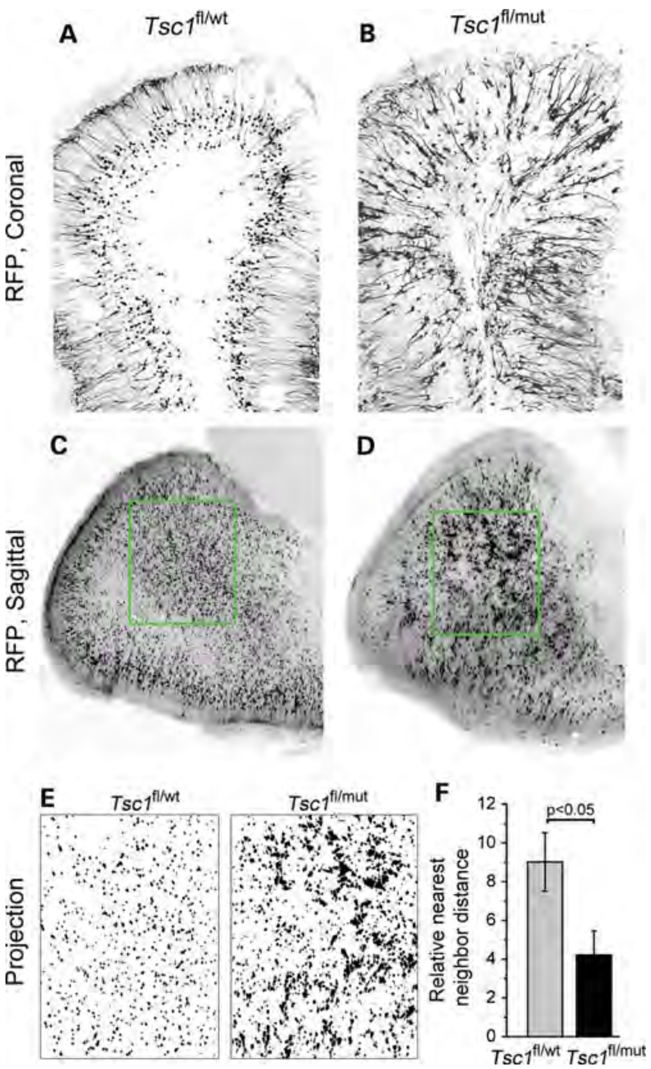

Figure 6. *Tsc1*^{null} neurons form micronodules throughout the olfactory bulb. Confocal images of RFP$^+$ cells in olfactory bulb coronal (**A** and **B**) and sagittal (**C** and **D**) sections from *Tsc1*$^{fl/wt}$/R26R (A and C) and *Tsc1*$^{fl/mut}$/R26R mice (B and D). (**E**) Projections of the RFP signals in the green square in (C) and (D). (**F**) The bar graph of the relative nearest neighbor distance for RFP$^+$ cells in the olfactory bulb of *Tsc1*$^{fl/wt}$/R26R (gray) and *Tsc1*$^{fl/mut}$/R26R (black) mice. Scale bars: 140 µm (A and B) and 200 µm (C and D).

along the RMS and the presence of neurons in the cortex that were absent in control mice. Although this strategy is efficient, it does not unambiguously identify SVZ cells as the source of the ectopic neurons and heterotopia. Second, we thus used *in vivo* electroporation to express Cre- and GFP-encoding plasmids selectively in SVZ cells resulting in *Tsc1* deletion when using *Tsc1*$^{fl/mut}$ mice. It is worth emphasizing that patients are born heterozygote for *Tsc1* or *Tsc2*. However, the heterozygote mice do not display any gross abnormalities (50). Considering that the SEGA in the SVZ have lost heterozygosity in TS patients (51), some of the cells generated from the SVZ are expected to be *Tsc1*^{null} or *Tsc2*^{null}. The following data emphasize that loss of heterozygosity is necessary for lesion formation.

Following *Tsc1* removal in neonatal neural progenitor cells and thus their progeny, we identified lesions as reported in TSC patients, in particular the heterotopias commonly called olfactory hamartomas (32,33). These heterotopias had either a mixed neuroglial or neuronal phenotype. The neuronal heterotopias contained cytomegalic, spiny neurons with enhanced mTOR activity and the presence of axons. The majority of these neurons were GFP$^+$, suggesting that they were born during the neonatal period (P1–10). The mixed neuroglial heterotopia contained a mixture of early born GFP$^+$/RFP$^+$ cells and GFP$^-$/RFP$^+$ cells born ~3–7 days prior to preparing brain sections (P28). These data suggest that the continual generation of cells from *Tsc1*^{null} SVZ neural progenitor cells leads to progressive accumulation of cells in the lesions and their subsequent increase in size. It remains unclear why some cells remains stalled along the migratory path. A premature differentiation as seen by the presence of cells with astrocytic and neuronal morphology could result in cell immobility. Alternatively, the presence of immature-looking cells with a radial-like morphology suggests that neural progenitor cells (i.e. radial glial cells) did not fully differentiate and remain stalled in the SVZ. Addressing this issue is outside the scope of this study. During migration, *Tsc1*^{null} neuroblasts displayed a slowed migration speed and a more complex morphology than *Tsc1*^{haplo} neuroblasts. Once in the olfactory bulb, *Tsc1*^{null} neurons formed micronodules, suggesting that their positional cues were altered. In addition, they displayed a hypertrophic dendritic tree consistent with a role of the mTOR pathway on dendritogenesis (52).

Another major finding is the presence of GFP$^+$ neurons in the cortex and nucleus accumbens around the anterior commissure. Cortical neurons were spiny and displayed morphologies reminiscent of pyramidal neurons. They also exhibited a thin process resembling an axon. Although only 10–15 were found per slice, they clustered in groups of 2–6 and could have a major impact on local circuit function. The function of these ectopic neurons will clearly warrant further investigation.

Our findings have major implications and raise important new questions. It is highly conceivable that *Tsc1*^{null} cells born along the SVZ around the time of birth in humans (neonatal period in mice) can generate olfactory lesions. In addition, because neural stem cells and neurogenesis persist in juvenile and adult humans (19,20,28), the continual generation of *Tsc1*^{null} cells from the SVZ in TSC patients may feed and increase in size the lesions that are formed neonatally or embryonically. Finding micronodules in the olfactory bulb raises the possibility that such abnormal structures may also be generated during embryonic life and would not be visible through conventional imaging. This finding together with the presence of ectopic neurons in the cortex and subcortical regions calls for closer examination of TSC tissue outside the tubers. Finally, TSC shares histological and clinical features with other disorders of cortical malformations such as focal cortical dysplasia and ganglioma that are associated with defects in neurogenesis (22). Collectively, we thus propose that neurogenesis along the SVZ progressively contributes to alterations in the forebrain during the neonatal and juvenile period resulting in progressive circuit disruption and perhaps neuropsychiatric instability in patients with TSC and other cortical malformations.

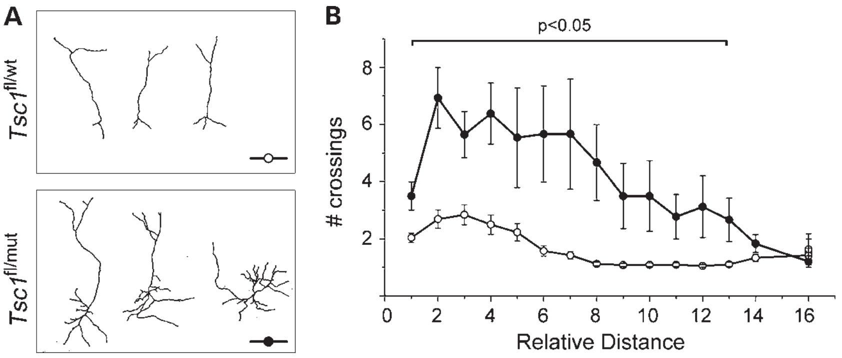

Figure 7. *Tsc1*^{null} neurons display a hypertrophic dendritic tree. (**A**) Representative reconstructions of RFP$^+$ olfactory neurons in sections from *Tsc1*$^{fl/wt}$/R26R and *Tsc1*$^{fl/mut}$/R26R mice. (**B**) Corresponding plots of the number of crossing as a function of the distance from the soma ($n = 14$ cells for each plot). Filled circles: *Tsc1*$^{fl/mut}$/R26R mice.

MATERIALS AND METHODS

Animals

Research protocols were approved by the Yale University Institutional Animal Care and Use Committee. Experiments were performed on littermate *Tsc1*$^{fl/wt}$/R26R and *Tsc1*$^{fl/mut}$/R26R mice obtained by crossing the following two lines of transgenic mice: *Tsc1*$^{fl/fl}$ (Jackson Laboratories) and *Ts1*$^{wt/mut}$ (NCI) that we had crossed with R26R-Stop-RFP mice (Jackson Laboratories, RFP for tdTomato). These two lines of mice were generated by David J. Kwiatkowski (Brigham and Women's Hospital, Harvard Medical School, Cambridge, MA, USA). For additional experiments, *Tsc1*$^{fl/fl}$ mice were crossed with nestin-CreER^{T2} mice (kind gift from Dr Amelia Eisch, UT Southwestern) that we had crossed with R26R-Stop-YFP mice (Jackson Laboratories) to generate *Tsc1*$^{fl/fl}$/nestin^{CreERT2} mice. Mice were prescreened for successful electroporation prior to sacrificing by viewing with an epifluorescence microscope or a Kodak 4000 imager.

Genotyping

Tail or toe samples were prepared using the standard protocols. We used previously published primers (53,54). The primer combination allows for the detection of the wt *Tsc1* allele at 295 bp, the fl allele at 480 bp and the mutant allele at 370 bp. The fl allele contains the LoxP sites surrounding the sequence to be excised upon Cre recombination. The mutant allele lacks the sequence flanked by LoxP sites, thus making the hamartin protein non-functional.

Neonatal electroporation

Electroporation is as we described previously (45,47). Plasmids (2–3 µg/µl) were diluted in phosphate buffered saline containing 0.1% fast green as a tracer; 0.5–1 µl of plasmid solution was injected into the lateral ventricles of cold-anesthetized neonatal pups using a pulled glass pipette (diameter <50 µm). Five square pulses of 50 ms duration with 950 ms intervals at 100 V were applied using a pulse ECM830 BTX generator and tweezer-type electrodes (model 520, BTX) placed on the heads of P0–1 pups.

Microdissection, RNA extraction and RT–PCR

Trizol reagent (750 µl) plus 200 µl of chloroform were added to each olfactory bulb sample and passed through a 22-gauge 1.5-inch needle and then vortexed. Following centrifugation for 15 min at 4°C and 12 000 *g*, the top aqueous phase was transferred to a fresh reaction tube. After adding 1000 µl of ethanol, the sample was vortexed for 1 min and centrifuged at 8000 *g* for 15 s. Pellets were rinsed three times with 75% ethanol. Following centrifugation, the RNA was eluted with RNase-free deionized H_2O prior to determining its concentration and purity on a spectrophotometer. The samples with contamination were subjected to an additional ethanol/sodium acetate precipitation.

For reverse transcription polymerase chain reaction (RT-PCR), 2.12 µg of RNA was mixed with deoxynucleotide triphosphates (dNTPs), random primers (Invitrogen) and RNase/DNase-free deionized H_2O, heated for 5 min at 65°C and then rapidly chilled on wet ice for 5 min, followed by brief centrifugation. Dithiothreitol, RNase out and SuperScript III were then added to each sample and reverse transcribed in a BioRad MyCycler. cDNA was then subjected to PCR using primers to *Tsc1* and *Gapdh*. Primer sequences are available upon request. mRNA transcripts were quantified by the standard curve method of qRT–PCR. cDNA was amplified with the specified primers and detected with SYBR Green (Bio-Rad) by a Chromogen-modified iCycler.

Genomic DNA isolation

Fresh, unfixed tissue was subjected to a proteinase K dilution and genomic DNA isolated using a DNeasy kit (DNA extraction). Quantification of DNA purity and concentration was performed, and ~0.19 µg of DNA was added to PCRs. 10× PCR buffer (Invitrogen) was added to 10 mM dNTP mix, 50 mM $MgSO_4$, autoclaved DNase-free deionized H_2O and Platinum Taq. The reaction volume was 25 µl after adding 1 µl of each forward and reverse primer with 3 µl of the appropriate sample. PCR was performed in a BioRad MyCycler (32–36 cycles). For recombination detection, 5 µl of product was subjected to a second round of PCR. Amplicons were visualized by running samples diluted in 10× blue juice DNA loading buffer loaded onto a 2% agarose gel run at 100 V for 30 min alongside a 100-bp DNA ladder (Invitrogen).

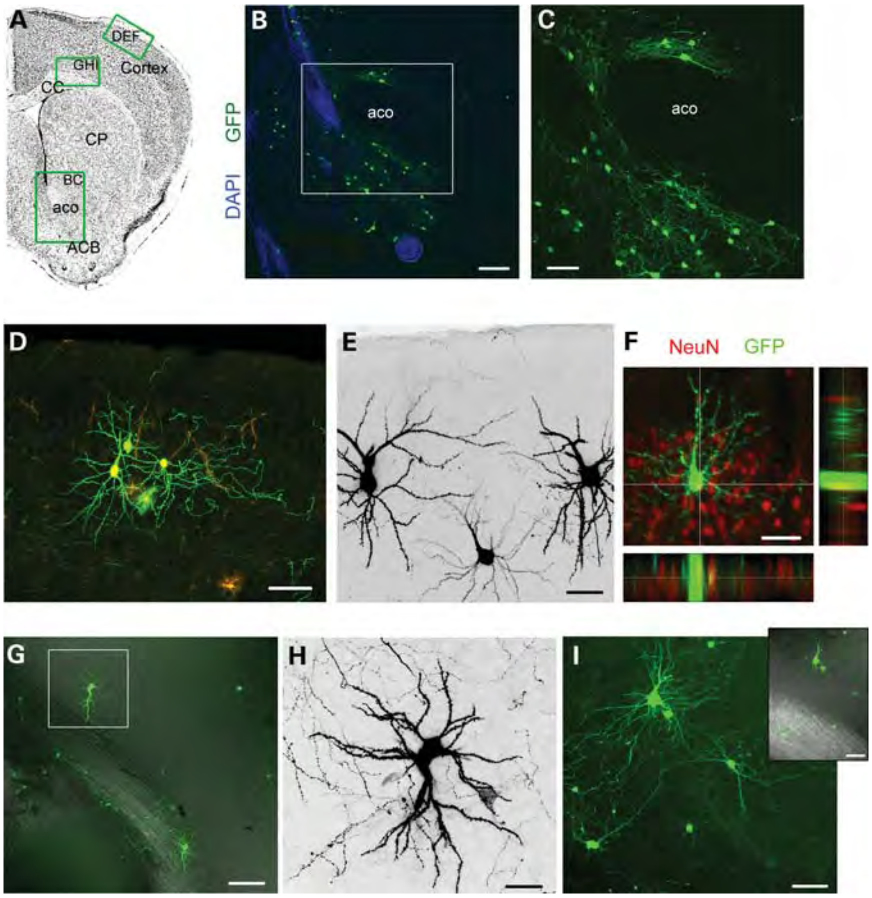

Figure 8. Newborn *Tsc1*^{null} neurons are rerouted to cortical and subcortical areas. (**A**) Coronal sections with green rectangles indicating the approximate locations of images shown in (**B**)–(**I**). (B) The confocal image of GFP$^+$ neurons (green) in the ACB and around the aco counterstained with DAPI (blue). (C) The zoom of the image in the white square in (B). (D) The confocal image of GFP$^+$ and RFP$^+$ neurons and astrocytes (bushy cells) in cortical layer II. (E) GFP$^+$ (black) neurons in cortical layer II. (F) The confocal image and projections of a GFP$^+$ cortical layer II cell that immunostained positive for NeuN (red). (G) The confocal image of GFP$^+$ neuron in the deep layer of the cortex. (H) Zoom of the neuron in the white square in (G). (I) The confocal image of GFP$^+$ neuron in the deep layer of the cortex. Inset: GFP fluorescence overlaid with DIC to illustrate the location of the corpus callosum. CC, corpus callosum; CP, caudate putamen; ACB, accumbens nucleus; aco, anterior commissure. Scale bars: 140 µm (B) 70 µm (C), 80 µm (D and G), 40 µm (E, F and I) and 30 µm (H).

Slice preparation and immunostaining

P28 mice were deeply anesthetized with pentobarbital (50 mg/kg). The brain was then quickly removed and placed in 4% paraformaldehyde overnight at 4°C, then washed in 1× PBS. The region of electroporation was imaged using a Kodak 4000 imager. The next day, 100-µm-thick slices were prepared using a vibratome (Leica VTS 1000). Immunostaining was performed in free-floating 100-µm-thick slices as described previously (55). Free-floating sections were blocked in PBS containing 0.1% Triton X-100, 0.1% Tween-20 and 2% bovine serum albumin and incubated in primary antibodies (see below) overnight at 4°C. After several washes in PBS containing 0.1% Tween-20, slices were incubated with the appropriate secondary antibody [Alexa Fluor series at 1:1000 (Invitrogen) or Cyanine series at 1:500 (Jackson ImmunoResearch)] for 1 h at room temperature. Primary antibodies were rabbit anti-pS6 (1:1000; Cell Signaling; S235/236, 2F9, catalog #4856), mouse anti-NeuN (1:500; Millipore), GFAP (1:100, DAKO) and DCX (1:500, Santa Cruz Biotechnology). Each staining was replicated in slices from three different mice. Z-section images were acquired on a confocal microscope (Olympus FluoView 1000) with a 20× dry objective (N.A. 0.75). Low-magnification images were acquired with a 10× dry objective or a dissecting scope (SZX16 with a SDF PLAPO 1× PF objective). Images were analyzed using Imaris 4.0 (Bitplane AG) and reconstructed using ImageJ 1.39t software (Wayne Rasband, NIH) or Photoshop CS3.

Cell size and pS6 immunostaining analyses

To measure cell size, Z-stack images of mRFP$^+$ cells in coronal sections were acquired with a 20× dry objective (Numerical Aperture, 0.75) using high–low settings to minimize saturation. In ImageJ, the freehand tracing tool was used to outline cell somas. Cell size was represented relative to the indicated controls. To measure nuclear size, Z-stack images of coronal sections stained for NeuN and DAPI were acquired with a 40× dry objective (Numerical Aperture, 1.20). Likewise, the freehand tracing tool was used to outline neuronal nuclei.

To measure mTOR activity, immunostaining was performed using an antibody to phosphorylated serine 235/236 of pS6. Serial Z-stacks were acquired under the same settings for the ipsilateral and contralateral coronal sections of an olfactory bulb. Regions of interest (ROIs) were generated using an elliptical selection tool, and average intensities for each ROI were determined. For both cell size and pS6 staining measurement, three sections per mouse were analyzed.

Acute slice migration assays

P21 mice were deeply anesthetized 20 mg/kg Nembutal and brains were dissected into ice-cold, oxygenated (95% O_2, 5% CO_2) high-glucose Dulbecco's modified eagle medium (DMEM). The 300 μm-thick sagittal slices were obtained using a Leica vibratome. After incubating for 1 h in room temperature DMEM, slices were transferred to a heated (35°C) perfusion chamber for 1 h. Individual fluorescently labeled cells in the RMS or RMS-OB were visualized using a confocal Olympus FluoView 1000 system. Confocal Z-stack images (4 μm spaced sections over 60–100 μm) were acquired with a 20× immersion objective (XUMPLFL, N.A. 1.20) every 5 min for at least 90 min. Movies were analyzed in ImageJ software (NIH). Image stacks were realigned and RFP-fluorescent cells were tracked using ImageJ plug-ins [Stackreg (56) and MTrackJ written by Dr E. Meijering, Biomedical Imaging Group Rotterdam]. Individual fluorescent cells were tracked using the MTrackJ plug-in. Cell migration speeds were calculated with a macro program as described previously (47,48).

Olfactory bulb organization

Sagittal slices were optically sectioned in the Z-plane at 4 μM intervals at a 4× magnification. Sections were stacked and converted to an 8-bit digital image followed by binary watershedding in ImageJ. Images were loaded and processed in geological image analysis software (GIAS v1.12, Beggan and Hamilton, 2010). Default settings were applied, and the nearest neighbor distance Ra was calculated. Organization is then measured as the theoretical Ra (based on a Poisson distribution) minus experimental Ra.

Morphometric analysis

Complete images of RFP^+ neurons were acquired in coronal sections using a Fluoview 1000 confocal microscope and 20× objective with a 2× digital zoom to focus on basal neurites. Neurites were traced with simple neurite tracer software (FIJI, GNU GPL v3). Scholl analyses were carried out using dendrite length as a measure of morphological complexity. Confocal Z-stacks from three different square fields of view were taken from each olfactory bulb section, and this was done for three different OB sections in a randomly selected series from each animal. At least three animals were analyzed per condition.

Statistics

Analysis of cell size and pS6 was performed on an average of 20–25 cells per slice, respectively, from 3 to 4 animals in each condition. The laminar distribution of cells was performed on 1–2 slices for 3–4 animals of each genotype. Data were presented in Origin 8.0. Statistical significance was determined using the unpaired Student's *t*-test or the Fisher's exact test when mentioned with $P < 0.05$ for significance (KyPlot 2.0). Data are presented as the mean ± SEM.

ACKNOWLEDGEMENTS

We thank Dr Amelia Eisch (UT Southwestern) for kindly providing the nestin-CreER^{T2} mice and Tiffany Lin for advice on using FIJI. The images of coronal brain sections were obtained from the Allen Brain Atlas.

Conflict of Interest statement. None declared.

FUNDING

This work was supported by grants from the Department of Defense (DoD, A.B.), a National Institutes of Health NRSA (grant number 10668225) and Epilepsy Foundation fellowship (D.M.F.).

REFERENCES

1. Osborne, J.P., Fryer, A. and Webb, D. (1991) Epidemiology of tuberous sclerosis. *Ann. N. Y. Acad. Sci.*, **615**, 125–127.
2. European Chromosome 16 Tuberous Sclerosis Consortium. (1993) Identification and characterization of the tuberous sclerosis gene on chromosome 16. *Cell*, **75**, 1305–1315.
3. Curatolo, P., Seri, S., Verdecchia, M. and Bombardieri, R. (2001) Infantile spasms in tuberous sclerosis complex. *Brain Dev.*, **23**, 502–507.
4. Holmes, G.L. and Stafstrom, C.E. (2007) Tuberous sclerosis complex and epilepsy: recent developments and future challenges. *Epilepsia*, **48**, 617–630.
5. Webb, D.W., Fryer, A.E. and Osborne, J.P. (1996) Morbidity associated with tuberous sclerosis: a population study. *Dev. Med. Child Neurol.*, **38**, 146–155.
6. Weiner, D.M., Ewalt, D.H., Roach, E.S. and Hensle, T.W. (1998) The tuberous sclerosis complex: a comprehensive review. *J. Am. Coll. Surg.*, **187**, 548–561.
7. Crino, P.B. (2004) Molecular pathogenesis of tuber formation in tuberous sclerosis complex. *J. Child Neurol.*, **19**, 716–725.
8. Crino, P.B., Aronica, E., Baltuch, G. and Nathanson, K.L. (2010) Biallelic TSC gene inactivation in tuberous sclerosis complex. *Neurology*, **74**, 1716–1723.
9. Feliciano, D.M., Su, T., Lopez, J., Platel, J.C. and Bordey, A. (2011) Single-cell Tsc1 knockout during corticogenesis generates tuber-like lesions and reduces seizure threshold in mice. *J. Clin. Invest.*, **121**, 1596–1607.
10. Thiele, E.A. (2004) Managing epilepsy in tuberous sclerosis complex. *J. Child Neurol.*, **19**, 680–686.
11. Uhlmann, E.J., Wong, M., Baldwin, R.L., Bajenaru, M.L., Onda, H., Kwiatkowski, D.J., Yamada, K. and Gutmann, D.H. (2002) Astrocyte-specific TSC1 conditional knockout mice exhibit abnormal neuronal organization and seizures. *Ann. Neurol.*, **52**, 285–296.
12. Meikle, L., Talos, D.M., Onda, H., Pollizzi, K., Rotenberg, A., Sahin, M., Jensen, F.E. and Kwiatkowski, D.J. (2007) A mouse model of tuberous sclerosis: neuronal loss of Tsc1 causes dysplastic and ectopic neurons, reduced myelination, seizure activity, and limited survival. *J. Neurosci.*, **27**, 5546–5558.
13. Way, S.W., McKenna, J. III, Mietzsch, U., Reith, R.M., Wu, H.C. and Gambello, M.J. (2009) Loss of Tsc2 in radial glia models the brain pathology of tuberous sclerosis complex in the mouse. *Hum. Mol. Genet.*, **7**, 1252–1265.
14. Zeng, L.H., Rensing, N.R., Zhang, B., Gutmann, D.H., Gambello, M.J. and Wong, M. (2010) Tsc2 gene inactivation causes a more severe epilepsy phenotype than Tsc1 inactivation in a mouse model of tuberous sclerosis complex. *Hum. Mol. Genet.*, **3**, 445–454.

15. Choi, Y.J., Di Nardo, A., Kramvis, I., Meikle, L., Kwiatkowski, D.J., Sahin, M. and He, X. (2008) Tuberous sclerosis complex proteins control axon formation. *Genes Dev.*, **22**, 2485–2495.
16. Mizuguchi, M. and Takashima, S. (2001) Neuropathology of tuberous sclerosis. *Brain Dev.*, **23**, 508–515.
17. Wei, J., Li, P., Chiriboga, L., Mizuguchi, M., Yee, H., Miller, D.C. and Greco, M.A. (2002) Tuberous sclerosis in a 19-week fetus: immunohistochemical and molecular study of hamartin and tuberin. *Pediatr. Dev. Pathol.*, **5**, 448–464.
18. Eriksson, P.S., Perfilieva, E., Bjork-Eriksson, T., Alborn, A.M., Nordborg, C., Peterson, D.A. and Gage, F.H. (1998) Neurogenesis in the adult human hippocampus. *Nat. Med.*, **4**, 1313–1317.
19. Curtis, M.A., Kam, M., Nannmark, U., Anderson, M.F., Axell, M.Z., Wikkelso, C., Holtas, S., Roon-Mom, W.M., Bjork-Eriksson, T., Nordborg, C. *et al.* (2007) Human neuroblasts migrate to the olfactory bulb via a lateral ventricular extension. *Science*, **315**, 1243–1249.
20. Wang, C., Liu, F., Liu, Y.Y., Zhao, C.H., You, Y., Wang, L., Zhang, J., Wei, B., Ma, T., Zhang, Q. *et al.* (2011) Identification and characterization of neuroblasts in the subventricular zone and rostral migratory stream of the adult human brain. *Cell Res.*, **11**, 1534–1150.
21. Zhao, C., Deng, W. and Gage, F.H. (2008) Mechanisms and functional implications of adult neurogenesis. *Cell*, **132**, 645–660.
22. Bordey, A. (2009) Neonatal progenitor contribution to epilepsy-associated cortical malformations. In Schwartzkroin, P.A. (ed.), *Encyclopedia of Basic Epilepsy Research*. Elsevier, Boston.
23. Pathania, M., Yan, L.D. and Bordey, A. (2010) A symphony of signals conduct early and late stages of adult neurogenesis. *Neuropharmacology*, **6**, 1060–1070.
24. Sanai, N., Tramontin, A.D., Quinones-Hinojosa, A., Barbaro, N.M., Gupta, N., Kunwar, S., Lawton, M.T., McDermott, M.W., Parsa, A.T., Manuel-Garcia, V.J. *et al.* (2004) Unique astrocyte ribbon in adult human brain contains neural stem cells but lacks chain migration. *Nature*, **427**, 740–744.
25. van den Berge, S.A., Middeldorp, J., Zhang, C.E., Curtis, M.A., Leonard, B.W., Mastroeni, D., Voorn, P., van de Berg, W.D., Huitinga, I. and Hol, E.M. (2010) Longterm quiescent cells in the aged human subventricular neurogenic system specifically express GFAP-delta. *Aging Cell*, **9**, 313–326.
26. Quinones-Hinojosa, A. and Chaichana, K. (2007) The human subventricular zone: a source of new cells and a potential source of brain tumors. *Exp. Neurol.*, **205**, 313–324.
27. Levison, S.W. and Goldman, J.E. (1993) Both oligodendrocytes and astrocytes develop from progenitors in the subventricular zone of postnatal rat forebrain. *Neuron*, **10**, 201–212.
28. van Strien, M.E., van den Berge, S.A. and Hol, E.M. (2011) Migrating neuroblasts in the adult human brain: a stream reduced to a trickle. *Cell Res.*, **11**, 1523–1525.
29. Shapiro, L.A., Ng, K.L., Kinyamu, R., Whitaker-Azmitia, P., Geisert, E.E., Blurton-Jones, M., Zhou, Q.Y. and Ribak, C.E. (2007) Origin, migration and fate of newly generated neurons in the adult rodent piriform cortex. *Brain Struct. Funct.*, **212**, 133–148.
30. De Marchis, S., Fasolo, A. and Puche, A.C. (2004) Subventricular zone-derived neuronal progenitors migrate into the subcortical forebrain of postnatal mice. *J. Comp. Neurol.*, **476**, 290–300.
31. Inta, D., Alfonso, J., von Engelhardt, J., Kreuzberg, M.M., Meyer, A.H., van Hooft, J.A. and Monyer, H. (2008) Neurogenesis and widespread forebrain migration of distinct GABAergic neurons from the postnatal subventricular zone. *PNAS*, **52**: 20994–20999.
32. Ridler, K., Suckling, J., Higgins, N., Bolton, P. and Bullmore, E. (2004) Standardized whole brain mapping of tubers and subependymal nodules in tuberous sclerosis complex. *J. Child Neurol.*, **19**, 658–665.
33. de Leon, G.A., Zaeri, N. and Foley, C.M. (1988) Olfactory hamartomas in tuberous sclerosis. *J. Neurol. Sci.*, **87**, 187–194.
34. Braffman, B.H., Bilaniuk, L.T., Naidich, T.P., Altman, N.R., Post, M.J., Quencer, R.M., Zimmerman, R.A. and Brody, B.A. (1992) MR imaging of tuberous sclerosis: pathogenesis of this phakomatosis, use of gadopentetate dimeglumine, and literature review. *Radiology*, **183**, 227–238.
35. Cusmai, R., Chiron, C., Curatolo, P., Dulac, O. and Tran-Dinh, S. (1990) Topographic comparative study of magnetic resonance imaging and electroencephalography in 34 children with tuberous sclerosis. *Epilepsia*, **31**, 747–755.
36. Gallagher, A., Chu-Shore, C.J., Montenegro, M.A., Major, P., Costello, D.J., Lyczkowski, D.A., Muzykewicz, D., Doherty, C. and Thiele, E.A. (2009) Associations between electroencephalographic and magnetic resonance imaging findings in tuberous sclerosis complex. *Epilepsy Res.*, **87**, 197–202.
37. Inoue, Y., Nemoto, Y., Murata, R., Tashiro, T., Shakudo, M., Kohno, K., Matsuoka, O. and Mochizuki, K. (1998) CT and MR imaging of cerebral tuberous sclerosis. *Brain Dev.*, **20**, 209–221.
38. Raznahan, A., Higgins, N.P., Griffiths, P.D., Humphrey, A., Yates, J.R. and Bolton, P.F. (2007) Biological markers of intellectual disability in tuberous sclerosis. *Psychol. Med.*, **37**, 1293–1304.
39. Bender, B.L. and Yunis, E.J. (1982) The pathology of tuberous sclerosis. *Pathol. Annu.*, **17**(Pt 1), 339–382.
40. Ess, K.C., Kamp, C.A., Tu, B.P. and Gutmann, D.H. (2005) Developmental origin of subependymal giant cell astrocytoma in tuberous sclerosis complex. *Neurology*, **64**, 1446–1449.
41. Zhou, J., Shrikhande, G., Xu, J., McKay, R.M., Burns, D.K., Johnson, J.E. and Parada, L.F. (2011) Tsc1 mutant neural stem/progenitor cells exhibit migration deficits and give rise to subependymal lesions in the lateral ventricle. *Genes Dev.*, **25**, 1595–1600.
42. Lagace, D.C., Whitman, M.C., Noonan, M.A., Ables, J.L., DeCarolis, N.A., Arguello, A.A., Donovan, M.H., Fischer, S.J., Farnbauch, L.A., Beech, R.D. *et al.* (2007) Dynamic contribution of nestin-expressing stem cells to adult neurogenesis. *J Neurosci.*, **27**, 12623–12629.
43. Shuang, M., Liu, J., Jia, M.X., Yang, J.Z., Wu, S.P., Gong, X.H., Ling, Y.S., Ruan, Y., Yang, X.L. and Zhang, D. (2004) Family-based association study between autism and glutamate receptor 6 gene in Chinese Han trios. *Am. J Med. Genet. B Neuropsychiatr. Genet.*, **131B**, 48–50.
44. Misson, J.P., Edwards, M.A., Yamamoto, M. and Caviness, V.S. Jr. (1988) Identification of radial glial cells within the developing murine central nervous system: studies based upon a new immunohistochemical marker. *Brain Res. Dev. Brain Res.*, **44**, 95–108.
45. Lacar, B., Young, S.Z., Platel, J.C. and Bordey, A. (2010) Imaging and recording subventricular zone progenitor cells in live tissue of postnatal mice. *Front Neurosci.*, **4**, 43.
46. Petreanu, L. and Alvarez-Buylla, A. (2002) Maturation and death of adult-born olfactory bulb granule neurons: role of olfaction. *J. Neurosci.*, **22**, 6106–6113.
47. Platel, J.C., Dave, K.A., Gordon, V., Lacar, B., Rubio, M.E. and Bordey, A. (2010) NMDA receptors activated by subventricular zone astrocytic glutamate are critical for neuroblast survival prior to entering a synaptic network. *Neuron*, **65**, 859–872.
48. Platel, J., Heintz, T., Young, S., Gordon, V. and Bordey, A. (2008) Tonic activation of GLUK5 kainate receptors decreases neuroblast migration in a whole mount preparation of the subventricular zone. *J. Physiol. (Lond.)*, **586**, 3783–3793.
49. Bolteus, A.J. and Bordey, A. (2004) GABA release and uptake regulate neuronal precursor migration in the postnatal subventricular zone. *J. Neurosci.*, **24**, 7623–7631.
50. Goorden, S.M., van Woerden, G.M., van der, W.L., Cheadle, J.P. and Elgersma, Y. (2007) Cognitive deficits in Tsc1+/- mice in the absence of cerebral lesions and seizures. *Ann. Neurol.*, **62**, 648–655.
51. Chan, J.A., Zhang, H., Roberts, P.S., Jozwiak, S., Wieslawa, G., Lewin-Kowalik, J., Kotulska, K. and Kwiatkowski, D.J. (2004) Pathogenesis of tuberous sclerosis subependymal giant cell astrocytomas: biallelic inactivation of TSC1 or TSC2 leads to mTOR activation. *J. Neuropathol. Exp. Neurol.*, **63**, 1236–1242.
52. Jaworski, J., Spangler, S., Seeburg, D.P., Hoogenraad, C.C. and Sheng, M. (2005) Control of dendritic arborization by the phosphoinositide-3′-kinase-Akt-mammalian target of rapamycin pathway. *J Neurosci.*, **25**, 11300–11312.
53. Kwiatkowski, D.J., Zhang, H., Bandura, J.L., Heiberger, K.M., Glogauer, M., el Hashemite, N. and Onda, H. (2002) A mouse model of TSC1 reveals sex-dependent lethality from liver hemangiomas, and up-regulation of p70S6 kinase activity in Tsc1 null cells. *Hum. Mol. Genet.*, **11**, 525–534.
54. Meikle, L., McMullen, J.R., Sherwood, M.C., Lader, A.S., Walker, V., Chan, J.A. and Kwiatkowski, D.J. (2005) A mouse model of cardiac rhabdomyoma generated by loss of Tsc1 in ventricular myocytes. *Hum. Mol. Genet.*, **14**, 429–435.
55. Platel, J.C., Gordon, V., Heintz, T. and Bordey, A. (2009) GFAP-GFP neural progenitors are antigenically homogeneous and anchored in their enclosed mosaic niche. *Glia*, **57**, 66–78.
56. Thevenaz, P., Ruttimann, U.E. and Unser, M. (1998) A pyramid approach to subpixel registration based on intensity. *IEEE Trans. Image Process*, **7**, 27–41.

Hypoxia-inducible factor 1a is a TSC1-regulated survival factor in newborn diseased neurons

Journal:	*Human Molecular Genetics*
Manuscript ID:	HMG-2012-W-00512
Manuscript Type:	1 General Article - US Office
Date Submitted by the Author:	27-Apr-2012
Complete List of Authors:	Feliciano, David; Yale University School of Medicine, Neurosurgery Zhang, Shiliang; Yale University School of Medicine, Neurosurgery Quon, Jennifer; Yale University School of Medicine, Neurosurgery Bordey, Angelique; Yale University School of Medicine, Celular and Molecular Physiology
Key Words:	tuberous sclerosis complex, Hif1a, neurogenesis, survival

Hypoxia-inducible factor 1a is a TSC1-regulated survival factor in newborn diseased neurons

David M. Feliciano, Shiliang Zhang*, Jennifer L. Quon*, and Angélique Bordey

Departments of Neurosurgery, and Cellular and Molecular Physiology, Yale University School of Medicine, New Haven, Connecticut, USA.

*: contributed equally.

Address for correspondence: Angélique Bordey, Ph.D.
Yale Univ. Sch. Med.
333 Cedar St, FMB 422
New Haven, CT 06520-8082
Phone: 203-737-2515
Fax: 203-737-2159
Email: angelique.bordey@yale.edu

Abstract

Tuberous Sclerosis Complex (TSC) is a genetic disorder caused by mutations in *Tsc1* or *Tsc2* resulting in hyperactivity of the mammalian target of rapamycin (mTOR) and disabling brain lesions. These lesions contained misplaced neurons enriched in hypoxia-inducible factor 1a (Hif1a). However, the relationship between TSC1/2 and Hif1a and the function of Hif1a in TSC neurons remain unexplored. Here, we examine the degree of Hif1a activity and its function in newborn *Tsc1*$^{\text{null}}$ neurons in a mouse model of TSC. Using single cell electroporation in the neurogenic subventricular zone (SVZ) of neonatal mice, we deleted *Tsc1* and generated olfactory lesions containing misplaced *Tsc1*$^{\text{null}}$ neurons. These newborn neurons displayed elevated Hif1a-mediated transcriptional activity compared to *Tsc1* heterozygote neurons and a marked resistance to cell death induced by a Hif1a antagonist. Electroporation of Hif1a targeting shRNA or dominant negative Hif1a constructs resulted in 80-90% loss of *Tsc1*$^{\text{null}}$ olfactory bulb granule cells and complete loss of ectopic neurons while sparing SVZ stem cells. Using an inducible shHif1a plasmid, we found that Hif1a is required for *Tsc1*$^{\text{null}}$ neuron survival at the inception of synaptic integration. Collectively, these results suggest that Hif1a acts as a molecular determinant of newborn neuron survival and that its TSC1-dependent up-regulation gave *Tsc1*$^{\text{null}}$ neurons a survival advantage despite their misplacement in a novel microenvironment.

Introduction

Tuberous Sclerosis Complex (TSC) is a developmental disorder caused by mutations in the tumor suppressor genes, *Tsc1* or *Tsc2*, resulting in benign growths, malformations, and neurological dysfunction [1-5]. Lesions within the central nervous system contain misplaced giant cells and neurons, which display increased activity of the mTOR signaling pathway [6, 7]. These diseased cells also display increases in the expression of the basic helix-loop-helix transcription factor hypoxia-inducible factor 1a (Hif1a) in human TSC tissue [8].

Hif1a is master transcriptional regulator of the adaptive response to hypoxia through activation of the transcription of many genes, including those involved in energy metabolism, angiogenesis, and apoptosis [9-11]. Through its transcriptional activity, Hif1a has been implicated in many vital cellular functions [11]. Recently, it was shown to regulate the proliferation and differentiation of adult neural stem cells in the hippocampal subgranular zone and the survival of retinal neurons during development [12, 13]. In TSC neurons, increased Hif1a expression is expected to result from mTOR hyperactivity since mTOR signaling pathway regulates Hif1a levels and activity in several systems [14]. Hif1a has also been shown to be elevated in $Tsc2^{null}$ and $Tsc1^{\mathrm{null}}$ mouse embryonic fibroblasts [15]. However, it remains to be examined whether *Tsc1* or *Tsc2* loss in neuronal cells leads to cell-autonomous increases in Hif1a expression and activity. In addition, the function of Hif1a in TSC neurons remains unknown.

Here, we examine Hif1a activity and function in newborn $Tsc1^{\mathrm{null}}$ neurons in a mouse model of TSC. In this model, *Tsc1* deletion in neonatal stem cells of the neurogenic subventricular zone (SVZ) through electroporation leads to olfactory bulb (OB) lesions containing ectopic $Tsc1^{\mathrm{null}}$ neurons. Using RT-PCR and *in vivo* gene reporter assays, we found that Hif1a levels and transcriptional activity were elevated in newborn *Tsc1*$^{\text{null}}$ neurons. Increasing Hif1a expression and activity in *Tsc1* heterozygote (*Tsc1*$^{\text{het}}$) neurons led to increase in their dendritic complexity. This finding may have important implications for neuronal development following exposure to a hypoxic environment like in preterm infants. Loss-of-function experiments using Hif1a shRNA or dominant negative constructs revealed that TSC1-dependent Hif1a up-regulation allows newborn *Tsc1*$^{\text{null}}$ neurons to survive within TSC lesions despite their placement in a heterotopic microenvironment.

Results

Generation of TSC-like lesions containing newborn *Tsc1*$^{\text{null}}$ neurons

To generate TSC-like lesions containing *Tsc1*$^{\text{null}}$ neurons, we used R26R$^{\text{RFP}}$ mouse pups containing a conditional (floxed, fl) and a wild type (wt) or *Tsc1* mutant (mut) allele (noted *Tsc1*$^{\text{fl/wt}}$ and *Tsc1*$^{\text{fl/mut}}$, **Fig. 1A**). CRE recombinase (CRE) and enhanced GFP-encoding DNA plasmids were injected into neural progenitor cells of the SVZ in postnatal day (P) 0-1 pups followed by electroporation (**Fig. 1B**). Neural progenitor cells are known to divide and generate transit amplifying cells that themselves generate neuroblasts. These neuroblasts migrate along the rostral migratory stream to reach the OB where they differentiate into interneurons, granule cells and periglomerular cells. Following CRE electroporation, we detected recombination at the R26R locus by visualizing RFP fluorescence in SVZ cells and in newborn neurons, which entered the OB circuitry by >10 days post-electroporation (dpe, P28 in **Fig. 1C**). As previously reported, we validated that *Tsc1* was knocked out in RFP^{+} neurons of *Tsc1*$^{\text{fl/mut}}$/R26R mice by immunostaining phosphorylated S6 in P28 OB sections (data not shown). S6 is phosphorylated by p70 S6Kinase 1, a downstream target of mTOR . Following CRE electroporation in *Tsc1*$^{\text{fl/mut}}$ mice, P28 OB contained heterotopia comprised of enlarged *Tsc1*$^{\text{null}}$ neurons that were not observed in *Tsc1*$^{\text{fl/wt}}$ mice (**Fig. 1C**).

Hif1a mRNA and transcriptional activity are up-regulated in newborn *Tsc1*$^{\text{null}}$ neurons

To examine Hif1a mRNA level, we performed endpoint RT-PCR from cDNA generated from CRE-electroporated (ipsilateral) and contralateral OB of P21 *Tsc1*$^{\text{fl/mut}}$/R26R mice. Five sets of primers were designed to amplify Hif1a mRNA transcripts using RT-PCR. Two of the five primers amplified the predicted size product with no genomic DNA contamination or primer dimers (**Fig. 2A**) and displayed single peak melt curves (data not shown). Both primer sets demonstrated increases in Hif1a transcripts in the OB containing *Tsc1*$^{\text{null}}$ neurons. To better quantify the increases, we performed quantitative (q) RT-PCR using the standard curve method with the most sensitive Hif1a primer set and GAPDH primer for normalization. There was a 3-fold increase in the Hif1a transcript levels in the OB containing *Tsc1*$^{\text{null}}$ neurons compared to the contralateral OB (**Fig. 2B**, N=6 mice for each condition, $p<0.05$). This increase is likely underestimated because of the low percentage of RFP^{+} neurons in the OB.

Hif1a forms a heterodimer with ARNT and regulates transcriptional activity of genes containing HIF response elements (HRE) within the promoter. We thus examined whether Hif1a-dependent gene transcription was increased in the OB containing *Tsc1*$^{\text{null}}$ neurons. We performed *in vivo* gene reporter assays by co-electroporating plasmids encoding CRE, a constitutively active renilla luciferase, or photinus pyralis luciferase under the control of HRE in *Tsc1*$^{\text{fl/mut}}$/R26R and *Tsc1*$^{\text{fl/wt}}$/R26R mice (**Fig. 2C**). The HRE-luciferase gene reporter activity was significantly increased in P28 OB containing *Tsc1*$^{\text{null}}$ neurons compared to OB containing

Tsc1^{het} neurons (**Fig. 2D**, n=18, p<0.001, mean= 3.1 vs. 0.4). Collectively, these experiments show that *Tsc1* deletion in newborn neurons is sufficient to increase Hif1a levels and induce transcriptional transactivation.

Hif1a overexpression increases the dendritic complexity of newborn neurons

To determine the function of supraphysiological levels of Hif1a, we performed postnatal electroporations of a Hif1a overexpression vector in SVZ cells of *Tsc1*$^{wt/mut}$ mice. For control, a GFP-encoding vector was electroporated. When these vectors were co-electroporated with HRE or constitutively active luciferase gene reporters, we found that Hif1a overexpression produced a significant 4-fold increase in HRE transcriptional activation in P28 OB compared to GFP expression (p<0.001, n=11 and 6, respectively, **Fig. 3A**). Hif1a overexpression produced no obvious migratory defects (data not shown). Since *Tsc1* knockout has been reported to enhance dendrite complexity in the OB and cortex [13, 16], we performed sholl analysis of Hif1a- or GFP-expressing granule cell dendrites in P28 coronal OB sections. Hif1a overexpression induced a significant increase in basal dendrite complexity and length (n=23, N=3 for Hif1a and n=30, N=3, for GFP, **Fig. 3C-E**). Thus, Hif1a overexpression in *Tsc1*^{het} neurons is sufficient to induce transcriptional transactivation and increase the dendritic complexity of these newborn neurons.

Tsc1^{null} neurons are partially resistant to Echinomycin-induced cell death

To assess the role of Hif1a in newborn TSC neurons, the Hif1a antagonist, echinomycin [17], was injected into CRE/GFP-electroporated *Tsc1*$^{fl/wt}$/R26R and *Tsc1*$^{fl/mut}$/R26R mice. Injections of echinomycin (10ug/Kg, [18]) or vehicle were performed once a day for 4 days starting at P6 or P8 (**Fig. 4A**). Following an additional 9 days (*i.e.* P18 to P21), whole brain imaging revealed a significant decrease in GFP and RFP fluorescence in the OB of *Tsc1*$^{fl/wt}$/R26R mice compared to *Tsc1*$^{fl/mut}$/R26R mice (**Fig. 4B**). We thus counted the number of newborn GFP^{+} *Tsc1*^{het} or *Tsc1*^{null} neurons in the granule cell layer of OB coronal sections. Echinomycin treatment resulted in a ~80% and 40% decrease in the number of newborn *Tsc1*^{het} and *Tsc1*^{null} granule cells, respectively, compared with vehicle-treated mice (**Fig. 4C**, N=10-14, $p<0.001$). *Tsc1*^{null} neurons were thus more resistant to echinomycin treatment than *Tsc1*^{het} neurons. This finding is in agreement with the increased levels and activity of Hif1a in *Tsc1*^{null} neurons compared to *Tsc1*^{het} neurons (see Fig. 2). In addition, no significant difference in the density of GFP^{+} cells in the SVZ was observed between echinomycin and vehicle-treated mice (data not shown). These results suggest that despite being mildly resistant to echinomycin-induced cell death, Hif1a may be a prosurvival factor in *Tsc1*^{null} neurons.

Hif1a is essential for the survival of newborn *Tsc1*^{null} neurons

Echinomycin is mildly selective for Hif1a and may have other targets. We thus performed Hif1a loss-of-function experiments by electroporating vectors encoding shRNA targeting Hif1a (shHif1a) or a dominant negative form of Hif1a (dnHif1a). These vectors or control vectors were co-electroporated with CRE- and GFP-encoding plasmids into *Tsc1*$^{fl/mut}$/R26R mice (**Fig. 5A**). Following electroporation of either one or two shHif1a-encoding vectors, we found an absence of GFP fluorescence in the OB upon whole brain examination at P19 and P28 (**Fig. 5B** for P19). Closer examination of OB coronal sections revealed a drastic reduction in the number of GFP^{+} shHif1a-expressing *Tsc1*^{null} neurons per section compared to control (0-5 instead of >500 cells in control, N=16 at P28 and N=6 at P19, **Fig. 5C and D**). In the SVZ of the same mice, electroporated GFP^{+} cells persisted along the lateral ventricle (**Fig.**

5E). This latter result suggests that Hif1a had no effect on SVZ cell survival in agreement with the low levels of Hif1a immunostaining in the postnatal SVZ (data not shown). Electroporation of the dnHif1a also significantly reduced the number of *Tsc1*^{null} neurons in the OB compared to control (P17, $p<0.001$, N=11 and N=11, **Fig. 5F**) without an obvious change in the SVZ GFP^{+} cell density (data not shown). Collectively, these data suggest that Hif1a is required in a cell-specific manner for survival of newborn *Tsc1*^{null} neurons.

Hif1a is required for *Tsc1*^{null} neuron survival at the onset of synaptic integration

To circumvent any effects of Hif1a knockdown on SVZ neural progenitor cells, we used an inducible Cre-Lox based plasmid vector to express shHif1a at a precise developmental stage of neuroblasts. The vector, called pSico (*i.e.* plasmid for stable RNA interference conditional [19]) contains a U6 promoter followed by LoxP sites around a CMV promoter driving GFP acting as a Stop sequence prior to the shHif1a sequence or a non-coding sequence (**Fig. 6A**). Following co-electroporation of pSico and a vector encoding ^{ET2}Cre^{ERT2} (and a GFP-encoding reporter vector) in *Tsc1*$^{fl/mut}$/R26R mice, intraperitoneal tamoxifen applications are expected to allow timed shHif1a expression in pSico-containing newborn neurons.

Tamoxifen was injected 10 dpe when newborn neuroblasts are integrating in the OB circuitry (see diagram in **Fig. 6B**). Recombination at the R26R locus was observed by RFP expression in newborn neurons (data not shown). By two weeks post-tamoxifen injection (P24), the number of shHi1a/GFP^{+} *Tsc1*^{null} neurons was significantly reduced compared to control (*i.e.* in mice electroporated with pSico control, N=6 and 5, **Fig. 6C-E**). Taken together, these results indicate that Hif1a is uniquely required by newborn *Tsc1*^{null} neurons at the inception of synaptic integration.

Discussion

Here, our data show for the first time that Hif1a acts as a molecular determinant of newborn neuron survival in the context of TSC. This finding suggests that TSC1-dependent Hif1a up-regulation gave *Tsc1*$^{\mathrm{null}}$ neurons a survival advantage despite their ectopic location in a novel microenvironment. We also found that increases in Hif1a expression and activity led to marked increase in the dendritic complexity and basal dendrite length of *Tsc1*$^{\mathrm{het}}$ neurons.

We used a recently established neonatal model of TSC-like lesions. These lesions are located in the OB and along the route from the SVZ to the OB and recapitulate several aspects of the TSC lesions seen in patients [20]. Indeed, TSC patients exhibit olfactory bulb hamartoma or malformations [16, 21]. Although several models of TSC pathologies have been reported [13, 14, 20, 22-30], our neonatal model recapitulates the discrete nature of the human lesions and allows easy access to tissue containing lesions and *Tsc1*$^{\mathrm{null}}$ cells. The TSC-like lesions consisted of migratory heterotopias, which were a collection of misplaced *Tsc1*$^{\mathrm{null}}$ cells (neurons and glia) as well as ectopic clusters of *Tsc1*$^{\mathrm{null}}$ neurons. *Tsc1*$^{\mathrm{null}}$ neurons that reached the OB displayed hypertrophic dendritic tree and formed micronodules. Here, we illustrated olfactory heterotopias and misplaced enlarged neurons in the OB. OB containing *Tsc1*$^{\mathrm{het}}$ neurons did not display such lesions and appeared normal. We found that the transcript levels of Hif1a were significantly increased in the OB containing *Tsc1*$^{\mathrm{null}}$ cells compared to the contralateral OB. In addition, we measured the transcriptional activity of Hif1a using *in vivo* luciferase reporter assays and found a significant increase in Hif1a activity in the OB containing *Tsc1*$^{\mathrm{null}}$ cells compared to those containing *Tsc1*$^{\mathrm{het}}$ cells. These data are in agreement with published data showing increased Hif1a expression as well as increased protein expression of Hif1-dependent genes (*e.g*. VEGF) in human TSC tissue [8, 15, 31-35].

Considering that Hif1a activity was increased in *Tsc1*^{null} cells, we perform a gain-of-function experiment by electroporating a Hif1a-overexpression vector [12]. We found that Hif1a overexpression in newborn neurons led to a significant increase in the basal dendritic complexity and length. It is thus possible that increased Hif1a activity contributes to the hypertrophic dendritic tree observed in *Tsc1*^{null} neurons. These experiments were performed in *Tsc1* heterozygote mice since patients are mutant for *TSC1* or *TSC2*. However, these data are in agreement that Hif1a or hypoxia may regulate dendritic complexity when expressed in newborn neurons of wild-type mice [36, 37]. This finding is intriguing and may have significant implications in developmental conditions during which infants are exposed to hypoxic conditions, such as preterm infants. In such conditions, Hif1a levels are known to be increased and may impact dendritic development. In addition, hypoxic conditions can induce mTOR activity and seizures [38, 39]. Thus, those infants carrying TSC mutations may be at additional risk during preterm labor.

To assess Hif1a function on *Tsc1*^{null} neuron development, we pharmacologically blocked Hif1a and performed loss-of-function experiments. The former experiment revealed that *Tsc1*^{null} neurons are partially resistant to inhibition with echinomycin compared to *Tsc1*^{het} neurons. This is in agreement with the finding that *Tsc1*^{null} neurons have more Hif1a than *Tsc1*^{het} neurons. Nevertheless, knockdown of Hif1 or expression of dominant negative Hif1a led to a significant 80-90% reduction in the number of newborn *Tsc1*^{null} neurons. The number of *Tsc1*^{null} SVZ cells did not appear to be affected suggesting that changes in SVZ stem cells did not account for the loss of newborn neurons. To test this hypothesis, we used inducible vectors to selectively knockdown Hif1a when newborn neurons had had migrated to the OB thus by-passing the majority of SVZ stem cells. Hif1 knockdown in integrating new born *Tsc1*^{null} neurons also led to a dramatic reduction in their number in the OB. Based on these data we suggest that Hif1a is required for newborn *Tsc1*$^{\mathrm{null}}$ neuron survival in particular at the onset of synaptic integration. Collectively, we propose that up-regulation of Hif1a transcriptional activity in newborn neurons promotes the growth and persistence of TSC lesions.

Materials and Methods

Animals

Research protocols were approved by the Yale University Institutional Animal Care and Use Committee. Experiments were performed on littermate *Tsc1*$^{\mathrm{fl/wt}}$/R26R and *Tsc1*$^{\mathrm{fl/mut}}$/R26R mice of either gender obtained by crossing the following 2 lines of transgenic mice: *Tsc1*$^{fl/fl}$ (Jackson Laboratories) and *Tsc1*$^{wt/mut}$ (NCI) that we had crossed with R26R-Stop-RFP mice (R26R$^{\mathrm{RFP}}$, Jackson Lab, RFP for tdTomato). These 2 lines of mice were generated by David J. Kwiatkowski (Brigham and Women's Hospital, Harvard Medical School, Cambridge, Massachusetts, USA). Mice were prescreened for successful electroporation prior to sacrificing by viewing with an epifluorescence microscope or a Kodak 4000 imager.

Genotyping

Tail or toe samples were taken and were subjected to DNA isolation, PCR amplification using previously published primers (51,52) and amplicons separated by standard electrophoresis methods.

Vectors

The vectors pCAG-HIF1a, PBS/pU6-HIF1s RNAi plasmid 1, PBS/pU6- HIF1a RNAi plasmid 2, pCAG-GFP, pCAG-CRE, and pCAG-$^{\mathrm{ERT2}}$Cre$^{\mathrm{ERT2}}$ were purchased from Addgene (donated by Dr. C. Cepko). For conditional shRNA expression, the Cre-Lox conditional vector, pSico (Addgene, Dr. M. Jacks) was used to place the Hif1a shRNA behind the floxed-GFP cassette. The pSico plasmid was co-injected with the tamoxifen-inducible Cre-recombinase expression vector pCAG-^{ERT2}Cre^{ERT2} (Addgene, Dr. C. Cepko) as well as a pCAG-tdTomato (noted RFP) vector that was constructed using the pCMV-tdTomato vector from Clontech. Upon inducing ^{ERT2}Cre^{ERT2}-recombinase activity with tamoxifen, the EGFP cassette would recombine out and place shRNA sequence directly downstream from the U6 RNA promoter. The control vectors for shRNA contained an empty sequence.

Neonatal electroporation

Electroporations were performed as previously described [14, 20]. For postnatal electroporations, plasmids (2-3 μg/μl) were diluted in PBS containing 0.1% fast green as a tracer. 0.5-1 μl of plasmid solution was injected into the lateral ventricles of neonatal pups using a pulled glass pipette (diameter <50 μm). 5 square-pulses of 50 ms-duration with 950 ms-intervals at 100 V were applied using a pulse ECM830 BTX generator and tweezer-type electrodes (model 520, BTX) placed on the heads of P0-P1 pups.

Luciferase Assays

Mice from postnatal electroporations were anesthetized with Nembutal and decapitated. Olfactory bulbs were flash frozen in liquid nitrogen and placed in 1.5 ml ice cold lysis buffer and subjected to a dual luciferase assay (Promega) according to manufacturer's recommendations. Tissue was passed through a pre-chilled 20 gauge needle attached to a 1 ml syringe 10 times. Samples were centrifuged at 10,000 x g for 10 minutes at 4^{o}C. The supernatant was then placed on ice for approximately 15 minutes. 20 μl of sample was preloaded into 100 μl of luciferase assay substrate II and briefly mixed. The luminescence was measured in a TD 20/20

Luminometer (Turner Designs, Sunnyvale, CA). 100 µl stop and glo reagent was then added, mixed, and the luminescence from renilla reniformis was determined.

Slice preparation and immunostaining

Postnatal day (P) 28 mice were deeply anesthetized with pentobarbital (50 mg/kg). The brain was then quickly removed and placed in 4% paraformaldehyde overnight at 4°C, then washed in 1x PBS. The region of electroporation was imaged using a Kodak 4000 imager. The next day, 100-µm-thick slices were prepared using a vibratome (Leica VTS 1000). Immunostaining was performed in free-floating 100-µm-thick slices as previously described (53). Free-floating sections were blocked in PBS containing 0.1% Triton X-100, 0.1% Tween-20, and 2% BSA and incubated in primary antibodies (see below) overnight at 4°C. After several washes in PBS containing 0.1% Tween-20, slices were incubated with the appropriate secondary antibody (Alexa Fluor series at 1:1,000 [Invitrogen]; or Cyanine series at 1:500 [Jackson ImmunoResearch]) for 1 hour at room temperature. Primary antibodies were rabbit anti-pS6 (1:1,000; Cell Signaling; S235/236, 2F9, catalog #4856) and Hif1a (1:500, Abcam). Each staining was replicated in slices from 3 different mice. Z-section images were acquired on a confocal microscope (Olympus FluoView 1000) with a 20X dry objective (N.A. 0.75). Low-magnification images were acquired with a 10x dry objective or a dissecting scope (SZX16 with a SDF PLAPO 1X PF objective). Images were analyzed using Imaris 4.0 (Bitplane AG) and reconstructed using ImageJ 1.39t software (Wayne Rasband, NIH) or Photoshop CS3.

Cell Counts

Cell number was determined by an observer blinded to conditions and genotypes in 1-3 slices per animal for several mice from multiple litters for each condition (for exact n, see text). 4 µm Z-sections were taken with a 10X dry objectives with a confocal microscope (Olympus

FluoView 1000) with a 1024 x 1024 resolution. Images were opened with image J and Z-projections were generated from each fluorescent channel. The stacked image was inverted, subjected to thresholding, and converted to a binary image. The image was then processed using image J watershedding. Blinded automated computational analysis was then performed (pixel area = 0.001-0.02, circularity = 0.5-1.0).

RNA isolation and quantitative (q) RT-PCR

RNA isolation and qRT-PCR were performed as described by Feliciano et al. [20]. Briefly, Trizol reagent and 21% chloroform were added to each electroporated olfactory bulb and passed through a 22 gauge 1.5 inch needle and then vortexed. Following centrifugation for 15 minutes at 4°C and 12,000 *g*, the top aqueous phase was transferred to a fresh reaction tube. After adding 1.0 ml of ethanol, the sample was vortexed for 1 minute, and centrifuged at 8,000 *g* for 15 seconds. Pellets were rinsed three times with 75% ETOH. Following centrifugation, the RNA was eluted with RNase-free deionized H_2O prior to determining its concentration and purity on a spectrophotometer. The samples with contamination were subjected to an additional ethanol/sodium acetate precipitation.

For RT-PCR, 2.12 µg of RNA was mixed with dNTPs, random primers (Invitrogen), and RNase/DNase-free deionized H_2O, heated for 5 minutes at 65°C, and then rapidly chilled on wet ice for 5 minutes, followed by brief centrifugation. DTT, RNase out, and SuperScript III were then added to each sample and reverse transcribed in a BioRad MyCycler. cDNA was then subjected to PCR using primers to *Hif1 (*F725, TGGTGCTAACAGATGACGGCGA; R1010, CCCGTGCAGTGAAGCACCTTCC; F401, GACAACGCGGGCACCGATTC; R665, TCACTGTCTAGACCACCGGATC*)*and *Gapdh* [14]. mRNA transcripts were quantified by the standard curve method of qRT-PCR. cDNA was amplified with the specified primers and detected with SYBR Green (Bio-Rad) by a Chromogen-modified iCycler.

Morphometric analysis

Complete images of RFP^+ neurons were acquired in coronal sections using a Fluoview 1000 confocal microscope and 20X objective with a 2x digital zoom to focus on basal neurites. Neurites were traced with simple neurite tracer software (FIJI, GNU GPL v3). Scholl analyses were carried out using dendrite length as a measure of morphological complexity. Confocal Z-stacks from 3 different square fields of view were taken from each olfactory bulb (OB) section. This was done for 3 different OB sections in a randomly selected series from each animal. At least 3 animals were analyzed per condition.

Statistics

Analysis was performed on 3-6 animals in each condition. Data were presented in Sigma Plot 11.0. Statistical significance was determined using unpaired Student t-test with $p<0.05$ for significance. Data are presented as mean ± standard error of the mean (SEM).

Acknowledgements: This work was supported by grants from the Department of Defense (Idea development award, W81XWH-10-1-0041, A.B), a National Institute of Health NRSA 10668225 and Epilepsy Foundation fellowship (D.M.F). We thank the lab members for helpful discussion and comments.

References:

1. Cheadle, J.P., et al., *Molecular genetic advances in tuberous sclerosis.* Hum Genet, 2000. **107**(2): p. 97-114.
2. Crino, P.B., K.L. Nathanson, and E.P. Henske, *The tuberous sclerosis complex.* N Engl J Med, 2006. **355**(13): p. 1345-56.

3. Curatolo, P., R. Bombardieri, and S. Jozwiak, *Tuberous sclerosis.* Lancet, 2008. **372**(9639): p. 657-68.
4. Tsai, P. and M. Sahin, *Mechanisms of neurocognitive dysfunction and therapeutic considerations in tuberous sclerosis complex.* Curr Opin Neurol, 2011. **24**(2): p. 106-13.
5. Ehninger, D., P.J. de Vries, and A.J. Silva, *From mTOR to cognition: molecular and cellular mechanisms of cognitive impairments in tuberous sclerosis.* J Intellect Disabil Res, 2009. **53**(10): p. 838-51.
6. Miyata, H., A.C. Chiang, and H.V. Vinters, *Insulin signaling pathways in cortical dysplasia and TSC-tubers: tissue microarray analysis.* Ann Neurol, 2004. **56**(4): p. 510-9.
7. Baybis, M., et al., *mTOR cascade activation distinguishes tubers from focal cortical dysplasia.* Ann Neurol, 2004. **56**(4): p. 478-87.
8. Parker, W.E., et al., *Enhanced epidermal growth factor, hepatocyte growth factor, and vascular endothelial growth factor expression in tuberous sclerosis complex.* Am J Pathol, 2011. **178**(1): p. 296-305.
9. Wang, G.L. and G.L. Semenza, *Characterization of hypoxia-inducible factor 1 and regulation of DNA binding activity by hypoxia.* J Biol Chem, 1993. **268**(29): p. 21513-8.
10. Wang, G.L. and G.L. Semenza, *General involvement of hypoxia-inducible factor 1 in transcriptional response to hypoxia.* Proc Natl Acad Sci U S A, 1993. **90**(9): p. 4304-8.
11. Semenza, G.L., *Hypoxia-inducible factors in physiology and medicine.* Cell, 2012. **148**(3): p. 399-408.
12. Chen, B. and C.L. Cepko, *HDAC4 regulates neuronal survival in normal and diseased retinas.* Science, 2009. **323**(5911): p. 256-9.
13. Fu, C., et al., *GABAergic Interneuron Development and Function Is Modulated by the Tsc1 Gene.* Cereb Cortex, 2011.
14. Feliciano, D.M., et al., *Single-cell Tsc1 knockout during corticogenesis generates tuber-like lesions and reduces seizure threshold in mice.* J Clin Invest, 2011. **121**(4): p. 1596-607.
15. Brugarolas, J.B., et al., *TSC2 regulates VEGF through mTOR-dependent and -independent pathways.* Cancer Cell, 2003. **4**(2): p. 147-58.
16. Ridler, K., et al., *Standardized whole brain mapping of tubers and subependymal nodules in tuberous sclerosis complex.* J Child Neurol, 2004. **19**(9): p. 658-65.
17. Kong, D., et al., *Echinomycin, a small-molecule inhibitor of hypoxia-inducible factor-1 DNA-binding activity.* Cancer Res, 2005. **65**(19): p. 9047-55.
18. Wang, Y., et al., *Targeting HIF1alpha eliminates cancer stem cells in hematological malignancies.* Cell Stem Cell, 2011. **8**(4): p. 399-411.
19. Nakamura, K., et al., *Brain-derived neurotrophic factor activation of TrkB induces vascular endothelial growth factor expression via hypoxia-inducible factor-1alpha in neuroblastoma cells.* Cancer Res, 2006. **66**(8): p. 4249-55.
20. Feliciano, D.M., et al., *Postnatal neurogenesis generates heterotopias, olfactory micronodules and cortical infiltration following single-cell Tsc1 deletion.* Hum Mol Genet, 2012. **21**(4): p. 799-810.
21. de Leon, G.A., N. Zaeri, and C.M. Foley, *Olfactory hamartomas in tuberous sclerosis.* J Neurol Sci, 1988. **87**(2-3): p. 187-94.

22. Meikle, L., et al., *A mouse model of tuberous sclerosis: neuronal loss of Tsc1 causes dysplastic and ectopic neurons, reduced myelination, seizure activity, and limited survival.* J Neurosci, 2007. **27**(21): p. 5546-58.
23. Goto, J., et al., *Regulable neural progenitor-specific Tsc1 loss yields giant cells with organellar dysfunction in a model of tuberous sclerosis complex.* Proc Natl Acad Sci U S A, 2011. **108**(45): p. E1070-9.
24. Zeng, L.H., et al., *Tsc2 gene inactivation causes a more severe epilepsy phenotype than Tsc1 inactivation in a mouse model of tuberous sclerosis complex.* Hum Mol Genet, 2011. **20**(3): p. 445-54.
25. Way, S.W., et al., *Loss of Tsc2 in radial glia models the brain pathology of tuberous sclerosis complex in the mouse.* Hum Mol Genet, 2009. **18**(7): p. 1252-65.
26. Magri, L., et al., *Sustained activation of mTOR pathway in embryonic neural stem cells leads to development of tuberous sclerosis complex-associated lesions.* Cell Stem Cell, 2011. **9**(5): p. 447-62.
27. Kim, S.H., et al., *Zebrafish model of tuberous sclerosis complex reveals cell-autonomous and non-cell-autonomous functions of mutant tuberin.* Dis Model Mech, 2011. **4**(2): p. 255-67.
28. Carson, R.P., et al., *Neuronal and glia abnormalities in Tsc1-deficient forebrain and partial rescue by rapamycin.* Neurobiol Dis, 2012. **45**(1): p. 369-80.
29. Govindarajan, B., et al., *Transgenic expression of dominant negative tuberin through a strong constitutive promoter results in a tissue-specific tuberous sclerosis phenotype in the skin and brain.* J Biol Chem, 2005. **280**(7): p. 5870-4.
30. Zhou, J., et al., *Tsc1 mutant neural stem/progenitor cells exhibit migration deficits and give rise to subependymal lesions in the lateral ventricle.* Genes Dev, 2011. **25**(15): p. 1595-600.
31. Menon, S., et al., *Chronic Activation of mTOR Complex 1 Is Sufficient to Cause Hepatocellular Carcinoma in Mice.* Sci Signal, 2012. **5**(217): p. ra24.
32. Duvel, K., et al., *Activation of a metabolic gene regulatory network downstream of mTOR complex 1.* Mol Cell, 2010. **39**(2): p. 171-83.
33. Kucejova, B., et al., *Interplay between pVHL and mTORC1 pathways in clear-cell renal cell carcinoma.* Mol Cancer Res, 2011. **9**(9): p. 1255-65.
34. El-Hashemite, N., et al., *Loss of Tsc1 or Tsc2 induces vascular endothelial growth factor production through mammalian target of rapamycin.* Cancer Res, 2003. **63**(17): p. 5173-7.
35. Zhang, C.Q., et al., *Expression and cellular distribution of vascular endothelial growth factor-C system in cortical tubers of the tuberous sclerosis complex.* Brain Pathol, 2012. **22**(2): p. 205-18.
36. Mazumdar, J., et al., *O2 regulates stem cells through Wnt/beta-catenin signalling.* Nat Cell Biol, 2010. **12**(10): p. 1007-13.
37. Pugh, P., et al., *Enhanced integration of newborn neurons after neonatal insults.* Front Neurosci, 2011. **5**: p. 45.
38. Cowan, F., et al., *Origin and timing of brain lesions in term infants with neonatal encephalopathy.* Lancet, 2003. **361**(9359): p. 736-42.
39. Cam, H. and P.J. Houghton, *Regulation of mammalian target of rapamycin complex 1 (mTORC1) by hypoxia: causes and consequences.* Target Oncol, 2011. **6**(2): p. 95-102.

Figures legends

Figure 1: Generation of TSC-like lesions containing newborn *Tsc1*$^{\mathbf{null}}$ neurons. (A) Transgenic mice electroporated with CRE- and GFP-encoding plasmids resulting in the generation of *Tsc1*$^{\mathrm{null}}$ and *Tsc* $^{\mathrm{het}}$ cells. **(B)** Diagram of a pipette containing DNA plasmid to be injected into the lateral ventricle and electroporated into SVZ cells (the SVZ is not shown). **(C)** Confocal image of GFP/RFP (white) and TOPRO-3 (red) fluorescence in a sagittal section of the olfactory bulb from a P28 *Tsc1*$^{\mathrm{fl/mut}}$/R26R mouse electroporated at P0 with CRE- and GFP-encoding plasmids. TOPRO-3 labels cell nuclei. Green arrows point to misplaced *Tsc1*$^{\mathrm{null}}$ neurons. The dotted blue line circles a heterotopia. Scale bar: 140 µm.

Figure 2: Hif1a mRNA and activity are up-regulated in newborn *Tsc1*$^{\mathbf{null}}$ neurons. (A) Diagram of coronal OB sections. The ipsilateral section contains GFP^{+}/RFP^{+} cells that contained CRE following electroporation at P1 in the SVZ. **(B)** PCR gels of Hif1a cDNA obtained from ipsilateral (CRE+) and contralateral (CRE-) P21 *Tsc1*$^{fl/mut}$ /R26R OB using two primer sets. **(C)** Bar graphs of the relative abundance of Hif1a mRNA measured by qRT-PCR and obtained from ipsilateral (CRE+) and contralateral OB from P28 *Tsc1*$^{fl/mut}$/R26R mouse. **(D)** Diagram of the luciferase vectors. **(E)** Bar graphs of the relative luciferase activity due to Hi1fa increase in CRE-containing OB from P28 *Tsc1*$^{\mathrm{fl/wt}}$ and *Tsc1*$^{\mathrm{fl/mut}}$ mice. *: $p<0.05$; **: $p<0.01$.

Figure 3: Hif1a overexpression increases the dendritic complexity of newborn neurons. (A) Diagram of the vectors used in *Tsc1*$^{\mathrm{wt/mut}}$ mice. **(B)** Bar graphs of the relative luciferase activity induced by Hi1fa overexpression in OB from P28 *Tsc1*$^{\mathrm{wt/mut}}$ mice. **(C)** Representative examples of traced basal dendrites from GFP (control)- or Hif1a-overexprressing granule cells. **(D)**

Number (#) of crossings as a function of the relative distance from traced control (while) and Hif1a-overexpressing (black) granule cells. **(E)** Bar graphs of the basal dendritic length in control and Hif1a-overexpressing cells. *: p<0.05; **: p<0.01.

Figure 4: *Tsc1*$^{\mathbf{null}}$ neurons are partially resistant to Echinomycin-induced cell death. (A) Diagram of the experimental protocol. **(B)** Images of P18 brain hemispheres from *Tsc1*$^{\mathrm{fl/mut}}$ and *Tsc1*$^{\mathrm{fl/wt}}$ mice following treatment with echinomycin. **(C)** Bar graphs of the relative number of *Tsc1*$^{\mathrm{null}}$ and *Tsc1*$^{\mathrm{het}}$ cells in the OB of *Tsc1*$^{\mathrm{fl/mut}}$ mice and *Tsc1*$^{\mathrm{fl/wt}}$, respectively, treated with either vehicle or echinomycin. *: p<0.05; **: p<0.01.

Figure 5: Hif1a is essential for the survival of newborn *Tsc1*$^{\mathbf{null}}$ neurons. (A) Diagram of the vectors used in *Tsc1*$^{\mathrm{fl/mut}}$/R26R mice. **(B)** Images of P19 brain hemispheres from control or shHif1a electroporated mice. **(C and D)** Confocal images of coronal P19 OB sections containing *Tsc1*$^{\mathrm{null}}$ cells expressing a control (C) or Hif1a shRNA (shHif1a) (D). shHif1a eliminated *Tsc1*$^{\mathrm{null}}$ neurons. **(E)** Confocal images of SVZ containing *Tsc1*$^{\mathrm{null}}$ cells expressing a control shRNA or shHif1a. Same mice as in (C and D). **(F)** Bar graphs of the relative number of *Tsc1*$^{\mathrm{null}}$ cells containing a control vector (grey) or dominant negative Hif1a (black). P<0.01.

Figure 6: Hif1a is required for *Tsc1*$^{\mathbf{null}}$ neuron survival at the onset of synaptic integration. **(A)** Diagram of the vectors used in *Tsc1*$^{\mathrm{fl/mut}}$/R26R mice. **(B)** Confocal images of coronal P24 OB sections containing *Tsc1*$^{\mathrm{null}}$ cells expressing control shRNA or shHif1a following induced expression at P10 with tamoxifen injections. **(C)** Bar graphs of the relative number of *Tsc1*$^{\mathrm{null}}$ cells containing either a inducible control shRNA (grey) or inducible shHif1a (black). P<0.001.

Figure 1, Feliciano

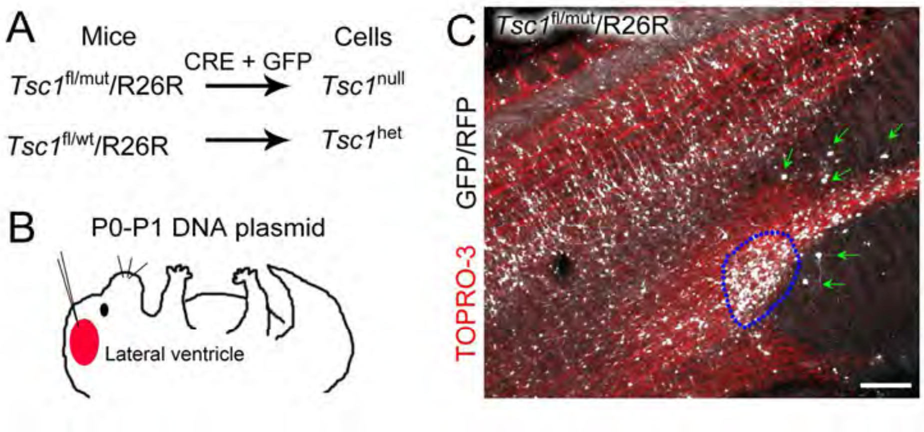

160x82mm (300 x 300 DPI)

Figure 2, Feliciano

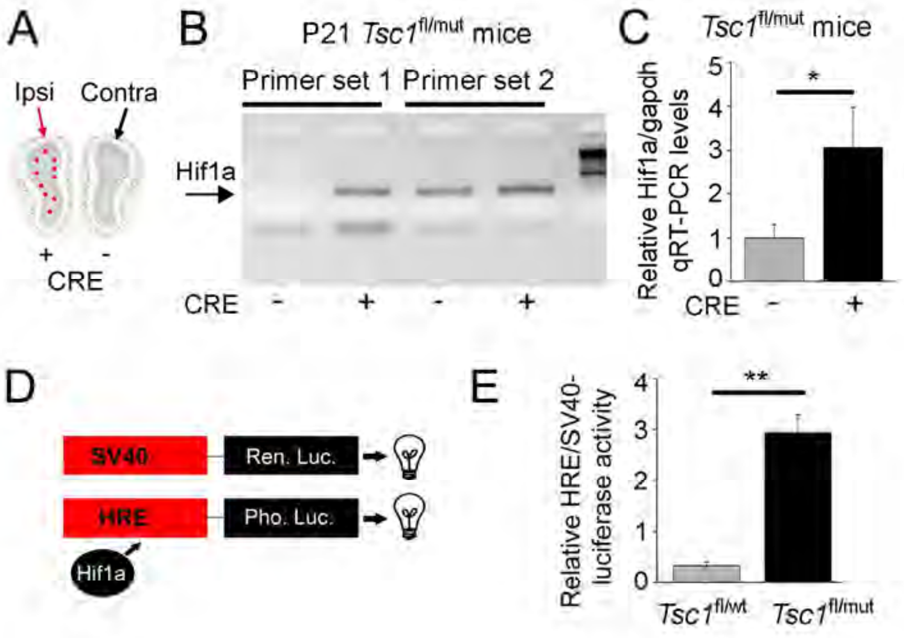

150x120mm (300 x 300 DPI)

Figure 3, Feliciano

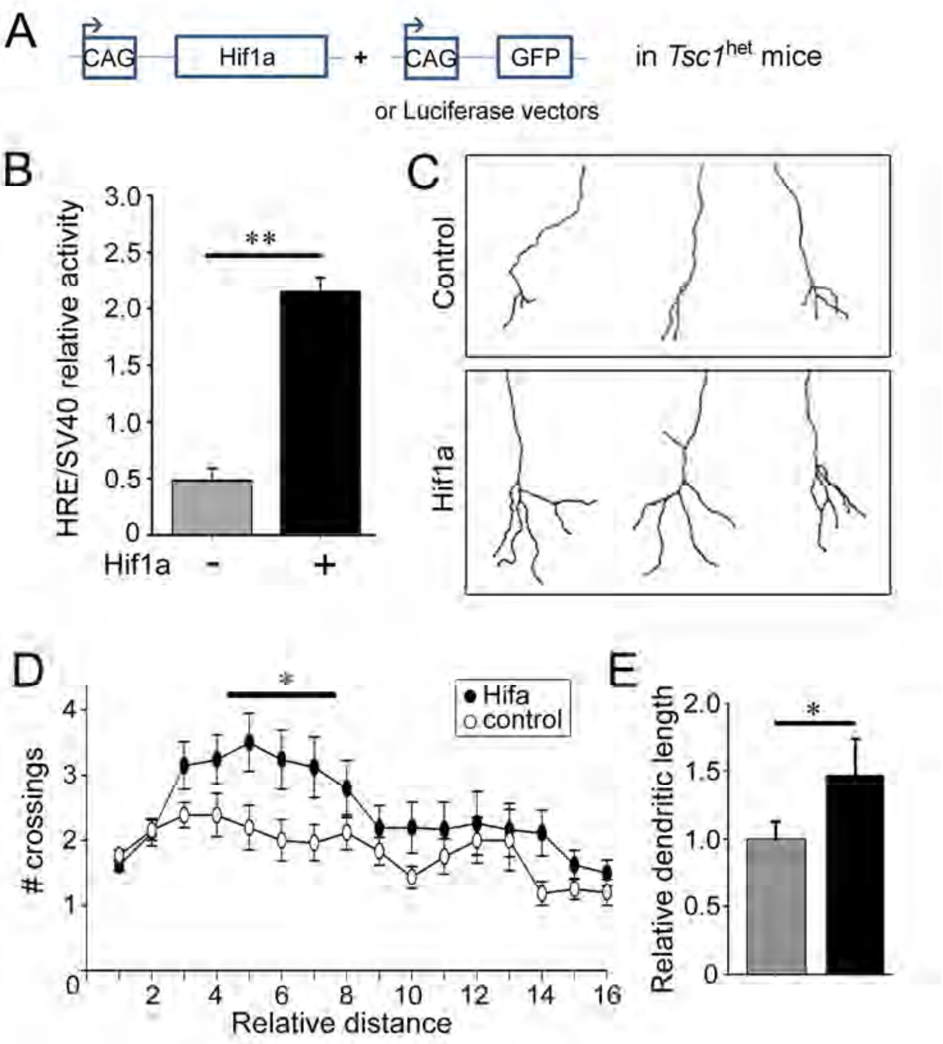

145x174mm (300 x 300 DPI)

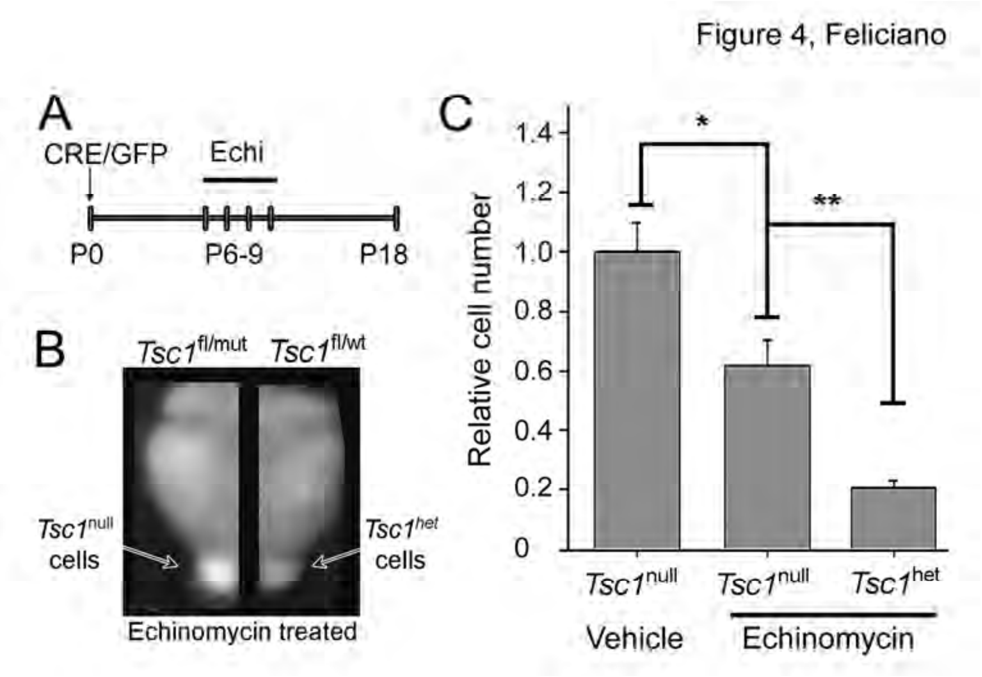

138x93mm (300 x 300 DPI)

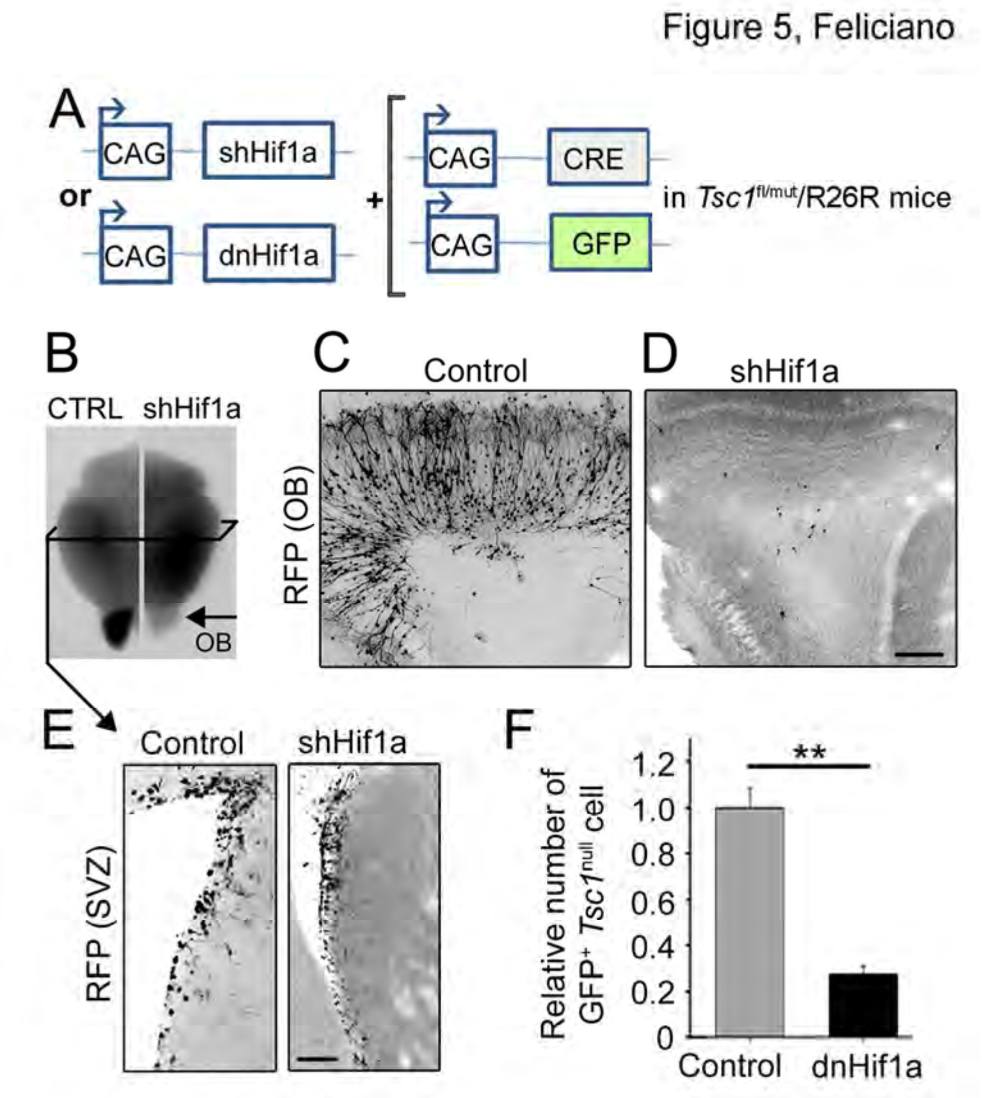

119x137mm (300 x 300 DPI)

Figure 6, Feliciano

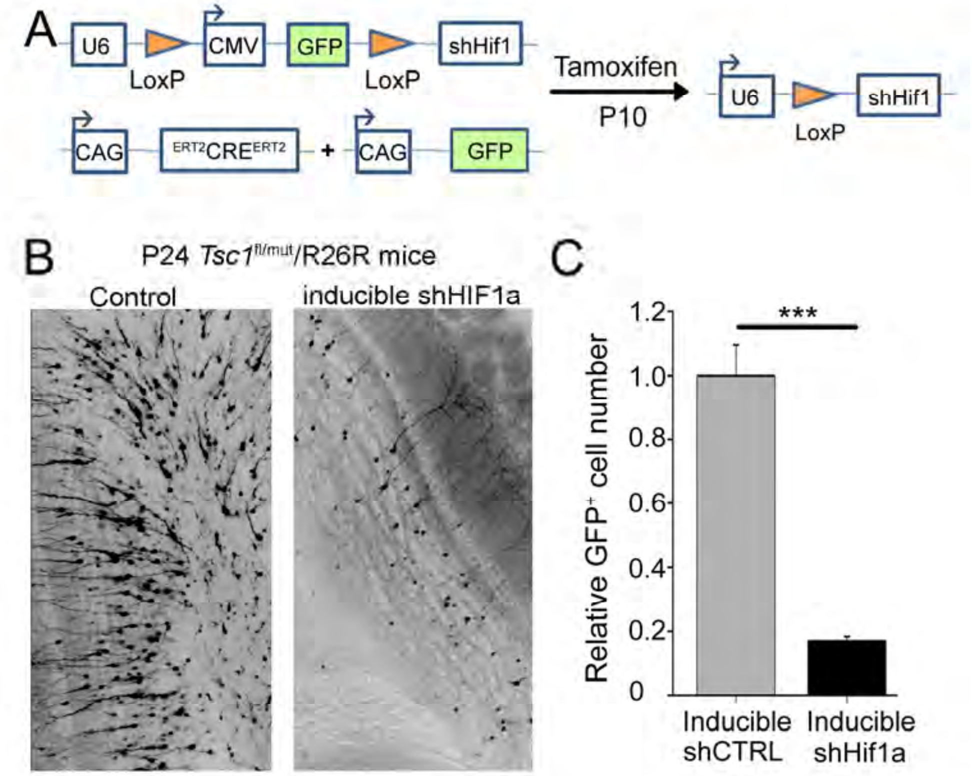

142x129mm (300 x 300 DPI)